Title: Sulfur Isotope Fractionation between Fluid and Andesitic Melt: An Experimental Study

Adrian Fiege[1,2], François Holtz[1], Nobumichi Shimizu[3], Charles W. Mandeville[4], Harald Behrens[1], Jaayke L. Knipping[1,2]

[1]Leibniz Universität Hannover, Institut für Mineralogie, Callinstraße 3, 30167 Hannover, Germany
[2]University of Michigan, Department of Earth and Environmental Sciences, 1100 North University Ave, Ann Arbor, MI 48109-1005, USA
[3]Woods Hole Oceanographic Institution, 266 Woods Hole Rd., Woods Hole, MS 23, MA 02543-1050, USA
[4]U.S. Geological Survey, 12201 Sunrise Valley Drive, Reston, MS 904, VA 20192, USA

E-mail: **afiege@umich.edu**, f.holtz@mineralogie.uni-hannover.de, nshimizu@whoi.edu, cmandeville@usgs.gov, h.behrens@mineralogie.uni-hannover.de, jaaykek@umich.edu

Fax: +49 511 762 3045
Phone: +49 511 762 5281

ABSTRACT

Glasses produced from decompression experiments conducted by Fiege et al. (2014a) were used to investigate the fractionation of sulfur isotopes between fluid and andesitic melt upon magma degassing. Starting materials were synthetic glasses with a composition close to a Krakatau dacitic andesite. The glasses contained 4.55 to 7.95 wt% H_2O, ~140 to 2700 ppm sulfur (S), and 0 to 1000 ppm chlorine (Cl). The experiments were carried out in internally heated pressure vessels (IHPV) at 1030°C and oxygen fugacities (fO_2) ranging from QFM+0.8 log units up to QFM+4.2 log units (QFM: quartz-fayalite-magnetite buffer). The decompression experiments were conducted by releasing pressure (P) continuously from ~400 MPa to final P of 150, 100, 70 and 30 MPa. The decompression rate (r) ranged from 0.01 to 0.17 MPa/s. The samples were annealed for 0 to 72 h (annealing time, t_A) at the final P and quenched rapidly from 1030°C to room temperature (T).

The decompression led to the formation of a S-bearing aqueous fluid phase due to the relatively large fluid-melt partitioning coefficients of S. Secondary ion mass spectrometry (SIMS) was used to determine the isotopic composition of the glasses before and after decompression. Mass balance calculations were applied to estimate the gas-melt S isotope fractionation factor $\alpha_{g\text{-}m}$.

No detectable effect of r and t_A on $\alpha_{g\text{-}m}$ was observed. However, SIMS data revealed a remarkable increase of $\alpha_{g\text{-}m}$ from ~0.9985 ± 0.0007 at >QFM+3 to ~1.0042 ± 0.0042 at ~QFM+1. Noteworthy, the isotopic fractionation at reducing conditions was about an order of magnitude larger than predicted by

previous works. Based on our experimental results and on previous findings for S speciation in fluid and silicate melt a new model predicting the effect of fO_2 on $\alpha_{g\text{-}m}$ (or $\Delta^{34}S_{g\text{-}m}$) in andesitic systems at 1030°C is proposed. Our experimental results as well as our modeling are of high importance for the interpretation of S isotope signatures in natural samples (e.g., melt inclusions or volcanic gases).

Keywords: Sulfur isotopes, SIMS, isotopic fractionation, fluid-melt, magma degassing, andesite

1. INTRODUCTION

Sulfur is a major volatile in volcanic systems and large amounts of S are released from magmas to fluid phases upon decompression. Thus, a good knowledge of the behavior of S and S isotopes during degassing as well as during magma-fluid interactions is required to improve our understanding of volcanic processes and, e.g., help monitoring and forecasting of volcanic eruptions. Sulfur is a polyvalent element and can be dissolved as S^{2-} and S^{6+} in silicate melts (e.g., Jugo et al., 2010; Metrich and Mandeville, 2010; Wilke et al., 2011), while the most relevant species in a fluid phase at magmatic conditions are SO_2 and H_2S (e.g., Katsura and Nagashima, 1974; Gerlach and Nordlie, 1975; Moretti et al., 2003).

Sulfur has four naturally occurring stable isotopes: ^{32}S (natural abundance: 95.04%), ^{34}S (4.20%), ^{33}S (0.75%), ^{36}S (0.01%); de Laeter et al. (2003). While considerable progress has been made in the past decades on the characterization of the partitioning of S between fluid and silicate melt at geologically relevant conditions (high *P* and *T*) and under fluid-melt equilibrium conditions (e.g., Keppler, 1999, 2010; Webster and Botcharnikov, 2011; Zajacz et al., 2012) as well as on the kinetics of S degassing (Fiege et al., 2014a), experimental data on fluid-melt S isotope fractionation are scarce (see review of Taylor, 1986).

S isotope fractionation between a silicate melt and a coexisting fluid phase depends on *T* and on the speciation of S in both phases (e.g., Sakai et al., 1982; Taylor, 1986). Ohmoto and Rye (1979) revealed the order $SO_4^{2-} > SO_3 > SO_2 > S^0 > H_2S > S^{2-}$ for the retention of ^{34}S in a S-bearing compound; i.e., the release of S from an oxidized melt where S is predominantly dissolved as SO_4^{2-} to a fluid phase is expected to result in isotopic enrichment of ^{34}S in the melt. Hence, the magnitude of S

isotope fractionation is strongly controlled by the redox conditions in the system (e.g., Sakai et al., 1982; Taylor, 1986; Mandeville, 2010). At oxidizing conditions the degassing of S upon decompression is dominated by SO_4^{2-} species in the melt and SO_2 in the fluid, while under reducing conditions the prevailing species are S^{2-} in the melt and H_2S in the fluid (e.g., Nagashima and Katsura, 1973; Carroll and Rutherford, 1988; Burgisser and Scaillet, 2007; Jugo et al., 2010). Thus, S isotope composition in the melt will progressively become heavier with S-degassing at oxidizing conditions and become lighter at reducing conditions if fluid and melt phase are in equilibrium. In theory, S isotope fractionation is approximately proportional to the relative mass difference of the considered S isotope pairs (e. g. ~2 amu difference between ^{34}S and ^{32}S) and proportional to $1/T^2$ (T in K, Faure, 1986; Mandeville, 2010).

S isotope analyses of natural samples were used in several studies published over the last decades to improve our understanding of high T magmatic processes (e.g., Marini et al., 1998; De Hoog et al., 2001; Labidi et al., 2012; de Moor et al., 2013). However, no experimental data has been produced in the last ~30 years. Fundamental experimental and theoretical studies by Richet et al. (1977), Sasaki et al. (1979), Ohmoto and Rye (1979), Ohmoto and Lasaga (1982), Sakai et al. (1982), Allard (1983), Ueda and Sakai (1984), Miyoshi et al. (1984) and Taylor (1986) provide the few relevant data so far for equilibrium S isotope fractionation between fluid and melt. More recent studies such as De Hoog et al. (2001), Mandeville et al. (2009) and de Moor et al. (2013) rely on the limited datasets from the 1970s and 1980s for equilibrium S isotope fractionation and their applicability to magmatic systems. Here, the work of de Moor (2013) helped significantly to improve our understanding of kinetic S isotope fractionation during volcanic degassing and their possible contribution to the S isotope signature that can be measured, e.g., in volcanic gases at the surface. Notably, the only existing experimental study conducted at magmatic T (800 to 1000°C), investigating the fractionation pairs SO_4^{2-} - S^{2-} and SO_4^{2-} - H_2S, was performed using molten salt (e.g., Na_2SO_4 and Na_2S; Miyoshi et al., 1984). The T dependence for the fluid-melt fractionation of S isotope has been summarized and discussed in the review of Taylor (1986) and the equations provided in that study were used by De Hoog et al. (2001) to develop a model for S isotope fractionation between fluid and melt. However, this model as well as the input parameters (e.g., the S isotope fractionation factors) have not been

tested experimentally at geologically relevant conditions (i.e., for silicate melts at high *P* and *T*). The absence of experimental calibration is related to the difficulties to determine quantitatively the S isotopic composition in silicate glasses. However, recent advances in the micro-analytical quantification of S isotopes in silicate glasses using SIMS allow us to analyze the S isotope composition in silicate glasses with S content of a few hundreds of ppm and with a precision of ~0.5 ‰ (Mandeville et al., 2008; 2010). Thus, it is now technically possible to determine isotope fractionation factors on experimental samples produced under magmatic conditions.

The present study is focused on the experimental investigation of S isotopes fractionation between (aqueous) fluid and andesitic melt. Considering that fluid phases in magmatic systems are commonly generated upon magma ascent (degassing), decompression experiments were conducted by Fiege et al. (2014a) to simulate natural degassing events. Here, we analyzed S isotopes in the glasses of selected samples from the experiments described by Fiege et al. (2014a) using SIMS to investigate the S fluid-melt fractionation. Based on our results and on existing models for S speciation in fluid and silicate melt a model is proposed to predict the isotopic distribution of S between andesitic melts and coexisting fluids.

2. EXPERIMENTAL PROCEDURE

Selected S-bearing glasses obtained from decompression experiments conducted by Fiege et al. (2014a) were used in this study. The isothermal decompression experiments were carried out at constant *T* (1030 ± 10°C) and variable fO_2 (QFM+0.8 to QFM+4.2; hereafter differences of log(fO_2) to the QFM buffer (Schwab and Küstner, 1981) are given to specify fO_2) in IHPV. The applied experimental approach is described in detail in Fiege et al. (2014a). Here, only the important information on the experimental procedure concerning the S isotope fractionation, studied in this work, are summarized.

The experimental strategy involves three steps: In the *first step* synthetic anhydrous glasses with a dacitic andesite composition close to the Krakatau dacitic andesite (Table 1) were prepared by melting a mixture of oxide and carbonate powders at 1600°C and 1 atm. In the *second step* ten volatile-bearing (H_2O, S, Cl) glasses were synthesized at high *P* (~500 MPa) and at 1030°C under fluid-undersaturated

conditions in an IHPV. These starting glasses were bubble-free and contained different amounts of H_2O (4.55 to 7.95 wt%) and S (260 to 2700 ppm, see Table 2). Three glasses also contained Cl (0.05 and 0.1 wt% Cl; Table 2). The isotopic composition of the starting glasses covers a wide range from $\delta^{34}S \approx$ -32 ‰ to about +23 ‰. The different $\delta^{34}S$ were adjusted by adding different S sources, either with known (IAEA standards: synthetic barite; see Section 3.2 for details) or with unknown S isotope composition (natural anhydrite, natural pyrrhotite or synthetic gypsum). The starting glasses GYClA, GYMClA and RED contained some S-bearing globules after the first high *P* annealing. Hence, a portion of these materials was re-melted to dissolve the globules and improve homogeneity (see Fiege et al. (2014a) for details concerning the re-melting procedure). In the *third step,* the volatile-bearing glasses were heated at 1030 ± 10°C and isothermal decompression experiments were conducted in IHPV by releasing *P* continuously from 400, 450 or 500 MPa to lower *P* (150 to 30 MPa) with different *r* ranging from ~0.02 to ~0.2 MPa/s. After decompression, the samples were either rapidly quenched to preserve eventually non-equilibrium conditions or annealed for various times (t_A = 1 to 72 h) at the final *P-T* conditions before quenching. The annealing at 1030°C after decompression was performed to approach near-equilibrium conditions between melt and fluid.

The nominal fO_2 prevailing in each experiment was either *i)* determined using the *Shaw*-membrane technique (e.g., Berndt et al., 2002; and references therein) or *ii)* estimated based on the known intrinsic redox conditions in the IHPV (Berndt et al., 2002; Wilke et al., 2002; Schuessler et al., 2008).

Table 1 and 2

3. ANALYTICAL APPROACH

3.1 Determination of major element and volatile concentrations in glasses.

The starting materials and the glasses of the decompression experiments were already characterized by Fiege et al. (2014a) using electron microprobe analyses (EMP; major elements, S, and Cl contents) and near infra-red (NIR) spectroscopy (H_2O contents). Details on the EMP and NIR measurements can be found in the Appendices A and B, respectively.

3.2 SIMS, data processing and determination of the fluid-melt isotopic fractionation of S.

The S isotope composition ($\delta^{34}S$; see below for details on the delta notation) of the andesitic glasses was determined by *in situ* SIMS using the Cameca IMS 1280 (mono-collector) of the Northeast National Ion Microprobe Facility (NENIMF) at Woods Hole Oceanographic Institution (WHOI). The measurements were conducted using a 10 µm Cs^+ primary beam, 10 kV accelerating voltage and 1-2 nA beam current. The secondary ions are collected at 10 kV accelerating voltage, 150 µm field of view and a mass resolution power (MRP) of 4000 to 5500, using an electron multiplier (EM). The energy slit is centered and opened to 40-60 V. Most samples were analyzed 2 to 8 times (see Table 2), depending on the quality of the measurements (e.g., the internal standard deviation), and each measurement consists of 50 cycles for ^{32}S and ^{34}S, respectively. The method of high precision *in situ* SIMS analysis of S isotopes in glasses down to a few hundreds of ppm of bulk S has been established recently at WHOI (Mandeville et al., 2008). Mandeville et al. (2008) demonstrated that by operating the Cameca IMS 1280 at mass resolving power of 5500 (M/ΔM), it is possible to avoid interferences from $^{31}P^{1}H$ with ^{32}S. The authors have shown that *in situ* $\delta^{34}S$ measurements (15 × 15 micron area) with a precision of ±0.4 to 0.6 ‰ can be conducted in silicate glasses containing about 500 to 1600 ppm S.

The analytical approach relies on the measurement of S-bearing glass standards with known S isotope composition to account for the instrumental fractionation. In-house glass standards at WHOI with major element compositions ranging from basaltic to high-silica glasses were used for this calibration (Appendix C; Mandeville et al., 2008). The S isotope composition of these glass standards ($\delta^{34}S_{true}$) covers a range from about -30 ‰ up to about +20 ‰ and was typically determined by conventional bulk methods (KIBA reagent extraction method; bulk S yield was always > 95% and typically ~98 %; for details see Appendix C and Sasaki et al., 1979; Ueda and Sakai, 1984; Mandeville et al., 2009) or calculated on the basis of the S isotope composition of the source of S for the glass syntheses (see below, this Section). Although the KIBA method has been criticized recently (Labidi et al., 2012), the high S yield (> 95%) and the nearly 1:1 correlation between the KIBA and the SIMS results (see Fig. C.1) confirm the high accuracy of our standard analyses. Furthermore, the linear relation between $\delta^{34}S_{true}$ and $\delta^{34}S_{measured}$ shows that matrix effects related to bulk composition (major element and S

isotope) or the oxidation state of S are negligible. Replicate analyses of a MORB glass standard (892-1) reveal an external reproducibility of SIMS analysis with a 2-standard error (n = 13) of ±0.52‰, which is consistent with observations of Mandeville et al. (2008). Details about the SIMS calibration for *in situ* S isotope analyses of silicate glasses are provided in Appendix C.

In addition, to monitor short and long term variations of the instrumental fractionation of the ion probe and to allow a correction of the raw isotopic data (see Appendix D for details), at least two measurements on a selected standard glass (usually MORB glass 892-1; $\delta^{34}S$ = 0.7 ± 0.3 ‰) were conducted after each 2-3 sample measurements. The accuracy of the analytical approach was also tested by using the IAEA standard materials SO-6 ($BaSO_4$; $\delta^{34}S$ = -31.1 ± 0.2 ‰; Halas and Szaran, 2001) and/or NBS-127 ($BaSO_4$; $\delta^{34}S$ = +20.3 ± 0.4 ‰; Hut, 1987; Halas and Szaran, 2001) as S source for the starting glasses SD1 (SO-6) and SD2 (~26.6 % NBS 127 and ~73.4 % SO-6; corresponding to a $\delta^{34}S$ of about -17.4 ‰). In SIMS measurements we found a $\delta^{34}S$ of -32.2 ± 0.4 ‰ for SD1 and a $\delta^{34}S$ of -16.6 ± 2.0 ‰ for SD2 (2 sigma errors). Thus, the S isotope composition of silicate glasses such as the experimental andesitic glasses of this study can be measured with an accuracy of ≤1 ‰ using *in situ* SIMS analyses. Details on the processing procedure of the raw SIMS data are given in Appendix D.

The corrected S isotope values of the decompressed glasses and the respective starting glass were used – together with the measured volatile contents in the melt – to determine the isotopic composition of the fluid phase and the isotopic fractionation factors via mass balance calculations for various fO_2 (ranging from ~QFM+1 to ~QFM+4). The S isotope composition is reported in a conventional delta (δ) notation given in ‰ (Table 2). The Vienna Canyon Diablo Troilite (V-CDT) was used as S isotope reference standard (Coplen and Krouse, 1998; Ding et al., 2001).

$$\delta^{34}S = \left(\left[\left({}^{34}S/{}^{32}S_{sample} \right) / \left({}^{34}S / {}^{32}S_{V\text{-}CDT} \right) \right] - 1 \right) \cdot 1000 \quad (1)$$

The gas-melt isotopic fractionation factor $\alpha_{g\text{-}m}$ was estimated using the following approximation:

$$\Delta^{34}S_{g\text{-}m} = \delta^{34}S_{gas} - \delta^{34}S_{melt} \approx 10^3 \ln \alpha_{g\text{-}m} \quad (2)$$

The measured and processed $\delta^{34}S$ of the starting glasses ($\delta^{34}S_{m\text{-}i}$) and of the partially degassed glasses of the decompression experiments ($\delta^{34}S_{m\text{-}f}$) were used to estimate $\delta^{34}S$ of the released fluid phase ($\delta^{34}S_{gas}$) via mass balance calculations (equations 3 and 4):

$$\delta^{34}S_{m\text{-}i} = f \cdot \delta^{34}S_{m\text{-}f} + (1 - f) \cdot \delta^{34}S_{gas} \quad (3)$$

$$\delta^{34}S_{gas} = [\delta^{34}S_{initial} - f \cdot \delta^{34}S_{melt}] / (1 - f) \quad (4)$$

where *f* represents the weight fraction of S remaining in melt after decompression, calculated from the S concentrations of the initial melt (i.e., of the starting glass) and of the partially degassed, decompressed melt. The S contents of the glasses were measured using electron microprobe and the analytical results as well as details on the analytical procedure are given in Fiege et al. (2014a).

3.2.1 SIMS analyses: Treatment of outliers

A few SIMS analyses were rejected due to strongly varying count statistics for ^{32}S and/or ^{34}S when measured on different locations on the same sample (and/or unexpected high or low counts when compared to experiments with similar S content in the glass). Hence, only one analysis was considered for the starting glass GYClA. These variations in count rates may reflect periodic instability of the primary beam during the analyses. However, considering that some samples were highly vesiculated, such a variation of count statistics can also be due to a contribution of S-bearing phases (i.e., quench phases from the fluid) at the bubble-melt interface to the detected S isotope signal. Notably, the strongly vesiculated sample SD2-1 could only be analyzed once owing to difficulties in identifying bubble-free spots that were large enough for SIMS analyses. The 2 sigma of the 50 analytical cycles is given as the error for these two samples (GYClA and SD2-1; see Table 2) and results related to these analyses were interpreted with caution.

Moreover, the uncertainty on the $\delta^{34}S$ of the starting glass AH is large compared to all other starting glasses ($\delta^{34}S$ of AH has 1 sigma error of ~2 ‰, Table 2), indicating heterogeneous S isotope

distribution. Thus, the low $\alpha_{g\text{-}m}$ values derived from the corresponding experiments (AH-3 and AH-4) have to be interpreted with caution. This is noted in the figure captions of all figures in which the results of the experimental series AH are plotted (Fig. 1 and 2). However, series AH will not be considered for the overall discussion of our data (Section 5 and following sections).

3.3 Determination of S speciation in melt and fluid using XANES spectroscopy

Fiege et al. (2014a) characterized the S speciation in most starting glasses and glasses of the decompression experiments via X-ray absorption near edge structure (XANES) spectroscopy at the S K-edge (2472 eV). Here, we performed additional XANES measurements with a smaller beam size (~60×60 µm instead of ~250×150 µm) to detect small scale variation in S speciation throughout an experimental sample, which may be attributed to contributions from the quenched phases in the bubbles to the spectra. Details on the XANES measurements can also be found in Appendix E.

4. RESULTS

The run products obtained after decompression consist of glass and bubbles with quenched fluids (decompression experiments) and no crystals could be detected. The experimental conditions and the volatile concentrations of starting glasses and of glasses after decompression are given in Table 2. The major element concentrations determined by EMP revealed that the glasses are chemically homogeneous and similar to the anhydrous dacitic andesite, if volatiles are subtracted and oxides are normalized to 100 wt% (see also Fiege et al., 2014).

4.1 Determination of $S^{6+}/\Sigma S$ and fO_2 in glasses using XANES spectra

The $S^{6+}/\Sigma S$ ratios in glasses determined by Fiege et al. (2014a) via XANES using the model of Jugo et al. (2010) are listed in Table 2. These values were used by Fiege et al. (2014a) to estimate the fO_2 inside the capsules [fO_2*(XANES)*] via equation 3 (see Section 5.2). The derived fO_2*(XANES)* values often differ significantly from the nominal fO_2 in the vessel. Possible reasons for these deviations are discussed in detail by Fiege et al. (2014a). As suggested by Fiege et al. (2014a) the nominal fO_2 is used to discuss and interpret the data obtained. However, fO_2*(XANES)* of some (reduced) samples is

applied (in addition to the nominal fO_2) to create a model predicting the effect of fO_2 on $\alpha_{g\text{-}m}$, in order to account for possible small differences between the nominal fO_2 in the vessel and within the capsule, which may have a significant effect on the S speciation in fluid- and melt-phase, respectively (see Section 5.2).

4.2 Sulfur speciation in the quenched fluid (XANES)

The results of the XANES measurements performed with a ~60×60 µm beam size are shown in the Appendix F. Areas containing high volume fraction of bubbles and areas nearly devoid of bubbles were selected and compared. Small differences between the spectra of bubble-bearing and bubble-free (or -poor) areas can be observed. Notably, the S fluid-melt partitioning data provided by Fiege et al. (2014a) for the same experiments shows that the S concentration in the fluid phase varies between ~1.7 and ~5.4 wt% at ~QFM+4 and between ~3.7 and ~4.7 wt% at ~QFM+1, while the S content measured in the quenched glasses is always < 0.12 wt% . XANES spectra collected on bubble-poor areas of oxidized samples (~QFM+4) indicate that the S in these glasses is almost exclusively present as sulfate S^{6+} (sharp peak at ~2482.2 eV), while spectra collected on areas with a high volume fraction of bubbles within the same sample reveal an additional, small but distinct peak at ~2478.2 eV, indicating the presence of sulfite S^{4+} (see, e.g., Backnaes et al., 2008; Wilke et al., 2008). On the other hand, under more reducing conditions (~QFM+1), a higher abundance of the broad peak at ~2477 eV observed for areas with a high volume fraction of bubbles when compared to spectra of bubble-poor areas, indicate a higher fraction of sulfide S^{2-} within the highly vesiculated part of the reduced samples (e.g., Jugo et al., 2010). Such variations can possibly be assigned to S species from the quench products of the fluid inclusions (see Appendix F for details). Hence, the XANES data indicate that SO_2 (S^{4+}) may be the prevailing S species in the fluid phase at QFM+4, while significant amounts of H_2S (S^{2-}) are probably present in the fluid at QFM+1 (see Fig. F.1 and description of spectra in Appendix F). Thus, the fluid-melt isotope fractionation of S at oxidizing conditions (> QFM+3) may be dominated by the isotopic fractionation pair $SO_{2\,(gas)} - SO_4^{2-}{}_{(melt)}$, while $H_2S_{(gas)} - S^{2-}{}_{(melt)}$ is probably the most relevant fractionation pair at reducing conditions ($\leq$ QFM+1; see also Marini et al. (1998),

Burgisser et al. (2008) and Jugo et al. (2010) for S speciation data). However, XANES spectra do not allow a quantitative estimation of the H_2S/SO_2 ratio in the fluid.

4.3 Sulfur isotope fractionation

A negative correlation between $\delta^{34}S_{melt}$ and the fraction of S remaining in the melt phase (*f*) under oxidizing conditions (> QFM+2.7) was found (see Fig. 1). The relative change in $\delta^{34}S_{melt}$ with increasing release of S seems to be independent on the initial isotopic composition which varied between -32‰ and +18‰ (Fig. 1). Hence, the instrumental S isotope fractionation as well as the gas-melt S isotope fractionation in natural systems is assumed to be largely independent of the (initial) S isotope composition of the glass, at least in the studied range of $\delta^{34}S_{melt}$. This is consistent with observations of Mandeville et al. (2008) for $\delta^{34}S_{melt}$ values ranging from -15‰ to +20‰. Thus, in the following, the initial $\delta^{34}S_{melt}$ will not be considered for the discussion and interpretation of detected fluid-melt isotope fractionation trends.

Fig. 2 shows a significant influence of fO_2 on the fluid-melt isotope fractionation. Although error bars are large for some experimental products, the dataset (see Table 2) confirms that the fluid-melt isotope fractionation of S is detectable with the applied experimental and analytical approach. In general, $\delta^{34}S_{melt}$ increases upon (S-) degassing at oxidizing conditions (~QFM+3), while it decreases at relatively reducing conditions (~QFM+1). This general observation is consistent with previous works and is directly related to the influence of fO_2 on the S speciation in the melt and the fluid phase (see, e.g., Taylor, 1986; de Moor et al., 2013). No significant fractionation is observed for the series of experiments performed at intermediate redox conditions (~QFM+1.8). The data in Fig. 1 and 2 show that the fluid has a lower $\delta^{34}S$ than the melt from which it exsolved at oxidizing conditions and higher $\delta^{34}S$ than the melt at reducing conditions, in agreement with the theoretical considerations (see review of Taylor, 1986). It is emphasized that data with different *r* and t_A shown in Fig. 2 are consistent; i.e., there is no detectable effect of these parameters on $\alpha_{g\text{-}m}$ (see next Section 4.3.1).

Figure 1 and 2

315 *4.3.1 Influence of t_A and r on $\alpha_{g\text{-}m}$*

316 In Fig. 3, $\alpha_{g\text{-}m}$ values of selected experimental series (GYClA, GYMClA and RED) are plotted against
317 t_A. The experimental series were chosen because they cover a wide range of t_A (0 h to ~20 h or ~72 h).
318 The data reveal that t_A has no significant influence on $\alpha_{g\text{-}m}$; i.e., $\alpha_{g\text{-}m}$ values of the same experimental
319 series are typically identical within error. This is consistent with the results obtained for
320 decompression experiments (using starting glass GYC) performed at different *r* and t_A = 0 h; i.e., $\alpha_{g\text{-}m}$
321 = 0.9989 ± 0.0015 at *r* ~0.16 MPa/s (experiment GYC-2) and $\alpha_{g\text{-}m}$ = 0.9985 ± 0.0013 at *r* ~0.05 MPa/s
322 (GYC-3). Thus, all $\alpha_{g\text{-}m}$ values given in Table 2 can be interpreted as reflecting equilibrium fluid-melt
323 fractionation. This also indicates that small changes in fO_2, which can be induced by decompression
324 (Burgisser and Scaillet, 2007) and, thus, may be expected in some experiments, do not necessarily
325 affect $\alpha_{g\text{-}m}$ values to a significant extent, at least if fO_2 is not close to the sulfide-sulfate transition.
326 Hence, even though S diffusion in the melt is probably the most important parameter controlling the
327 rate of S degassing to a fluid phase upon decompression (e.g., Nemec, 1980a; 1980b; Sparks et al.,
328 1994; Behrens and Stelling, 2011; Müller-Simon, 2011), the fluid-melt S isotope fractionation
329 observed in our experiment can be described by a single $\alpha_{g\text{-}m}$ value as long as fO_2, and, thus, the S
330 speciation in melt and fluid remains rather constant. However, kinetic S isotope fractionation effects
331 may play a significant role in degassing magmas which show larger bubble-bubble distances than
332 observed in our experimental run products (typically < 50 µm after decompression at ~0.1 MPa/s; see
333 also Fiege et al., 2014b) and a fast fluid separation after volatile exsolution (see de Moor et al., 2013).
334 On the other hand, the discrepancies between GYClA (average $\alpha_{g\text{-}m}$ = 1.0025 ± 0.0011) and GYMClA
335 (average $\alpha_{g\text{-}m}$ = 0.9986 ± 0.0011; see Fig. 3) are interpreted to reflect slight differences in fO_2 because
336 these experiment were conducted at fO_2 close to the sulfide-sulfate transition in silicate melts (see,
337 e.g., of Baker and Moretti, 2011; Moretti and Ottonello, 2005) and small variation in fO_2 may change
338 $\alpha_{g\text{-}m}$ significantly at these redox conditions (around ~QFM+1.8). Notably, the $\delta^{34}S$ of GYClA is based
339 on a single analysis (see Section 3.2.1), which could also explain the discrepancies because a change
340 of the $\delta^{34}S$ of GYClA by -2 to -3 ‰ would eliminate most differences.
341

342 Figure 3

343

344 *4.3.2 Influence of fO_2 on $\alpha_{g\text{-}m}$*

345 Fig. 2 and Fig. 3 indicate that the fluid-melt S isotope fractionation strongly depends on fO_2. The
346 whole dataset of $\alpha_{g\text{-}m}$ values given in Table 2 is reported as a function of ΔQFM in Fig. 4 except for
347 the results of experimental series AH, which have to be interpreted with caution (see Section 3.2.1).
348 Fig. 4 reveals that $\alpha_{g\text{-}m}$ is > 1 at log(fO_2/bar) < QFM+1.5 and < 1 at log(fO_2/bar) > QFM+2.5. The
349 redox range between QFM+1.5 and QFM+2.5, in which $\alpha_{g\text{-}m}$ changes from less than 1 to more than 1,
350 correlates well with the sulfide-sulfate transition in silicate melts (e.g., Jugo et al., 2010; Klimm et al.,
351 2012).
352 Three starting compositions also contained Cl and the results show that the presence of Cl in bulk
353 concentrations up to 1000 ppm has no measurable effect on the S isotope fractionation at ~ QFM+1.5.
354 The scattering of the data is mainly due to the analytical precision of the SIMS technique. Based on
355 the experimental data in Table 2, an average $\alpha_{g\text{-}m}$ of 0.9985 ± 0.0007 is derived for oxidizing
356 conditions at log(fO_2/bar) ≥ QFM+2.8 and an $\alpha_{g\text{-}m}$ of ~1.0042 ± 0.0024 is calculated for relatively
357 reducing redox conditions at log(fO_2/bar) ≈ QFM+1. It is emphasized that the fractionation factors for
358 a given fO_2 are identical within error if only experiments with t_A > 5 h or $r \leq 0.05$ MPa/s are
359 considered for the calculation of the mean values (~0.9988 ± 0.0013 at >QFM+4 and ~1.0032 ±
360 0.0027 at ~QFM+1), indicating that equilibrium isotopic distribution was attained in the experiments.

361

362 Figure 4

363

364 **5. DISCUSSION**

365 The results presented in this study provide first experimental constraints on the fractionation of S
366 isotopes between H_2O-S-(Cl)-fluids and silicate melts during magma degassing at geologically
367 relevant conditions. As mentioned above, the influence of r and t_A at final P on S isotope fractionation
368 is negligible within the investigated redox range. Hence, the observed influence of fO_2 on $\alpha_{g\text{-}m}$
369 probably reflect equilibrium isotope fractionation effects occurring upon closed system degassing,

even if experiments were directly quenched after decompression (t_A = 0 h). This is not surprising as kinetically controlled isotopic fractionation processes are rare in high *T* processes occurring in magmatic systems (O'Neil, 1986). Thus, our results indicate that S isotopic equilibrium between fluid and andesitic melt is reached during a degassing event, which is controlled by a *r* ranging from ~0.01 to 0.16 MPa/s. Notably, based on the same set of experiments, kinetically controlled degassing mechanisms were revealed by Fiege et al. (2014a) for the release of S from oxidized andesitic melt upon fast decompression. The authors noted that equilibrium distribution of S between fluid and melt was only reached after a t_A of ≥ 5 h at oxidizing conditions. Our SIMS measurements indicate that even during the transient release of large amounts of S upon decompression, observed by Fiege et al. (2014a), equilibrium fractionation of S between fluid and melt can be assumed.

5.1 Comparison with the De Hoog et al. (2001) model

In the following discussion, the new results are compared to the model of De Hoog et al. (2001), which is based on the modeling approach of Sakai et al. (1982) as well as experiments and theoretical considerations from the 1970s and early 1980s (summarized by Taylor, 1986). The $\Delta^{34}S_{g\text{-}m}$ values for each experiment, calculated following equation 2, were used to determine average $\Delta^{34}S_{g\text{-}m}$ values for each experimental series at a given fO_2 (e.g., GYB, GYC, etc.; see Table 2). Fig. 5 shows the (average) $\Delta^{34}S_{g\text{-}m}$ values in comparison to a trend predicted by the model of De Hoog et al. (2001) for 1030°C. The *De Hoog*-model underestimates the isotopic fractionation at reducing conditions by about one order of magnitude (i.e., by a factor of 3.6 to 15.6), while it reproduces the data at oxidizing conditions within the uncertainty. The significant discrepancies at reducing conditions may either be related to the modeling approach in the *De Hoog*-model or, more likely, to uncertainties of the input parameters; i.e., $\alpha_{g\text{-}m}$ values as well as the S speciation in the fluid and melt phase at given fO_2. The *De Hoog*-model relies on the *T* dependences of $\alpha_{g\text{-}m}$ provided by Miyoshi et al. (1984) and Taylor (1986) as well as on equations of Marini et al. (1998) and Wallace and Carmichael (1992) linking fO_2 to the speciation of S in the fluid and in the melt, respectively. The differences observed at ~QFM+1 indicate that one or both of the *T* dependences determined by Miyoshi et al. (1984) for $\alpha(SO_4^{2-}{}_{melt} - H_2S_{gas})$ and $\alpha(SO_4^{2-}{}_{melt} - S^{2-}{}_{melt})$, respectively, in the *T* range of 600 to 1000°C and used by De Hoog et al. (2001) for the

estimation of $\alpha(H_2S_{gas} - S^{2-}_{melt})$ may be not applicable for silicate melts at high *T* conditions (i.e., > 1000°C). We suggest, that the experimental data of Miyoshi et al. (1984) have to be applied with caution to silicate systems considering that the S isotope fractionation factor $\alpha(SO_4^{2-}_{melt} - H_2S_{gas})$ was determined between SO_4^{2-} in NaCl or LiCl-KCl melts and H_2S in an aqueous fluid and that $\alpha(SO_4^{2-}_{melt} - S^{2-}_{melt})$ was determined based on experiments in which anhydrous Na_2SO_3 was decomposed in NaCl or LiCl-KCl melts. Here, possible differences between $\alpha(SO_4^{2-}_{melt} - S^{2-}_{melt})$ in salt melts and $\alpha(SO_4^{2-}_{melt} - S^{2-}_{melt})$ in silicate melts at given *T* probably reflect a significant effect of the matrix composition on bonding energies because equilibrium (S) isotope fractionation is directly related to the effect of the atomic mass on bond energy (e.g., O'Neil, 1986). Considering that the predominant S species in oxidized salt and silicate melts are probably quite similar (e.g., $CaSO_4$ or Na_2SO_4 in silicate melts vs. K_2SO_4 or Na_2SO_4 in salt melts: see, e.g., Behrens and Stelling, 2011; Ayris et al. 2013), while the predominant S species in reduced Fe-bearing silicate melts is FeS (e.g., Zajacz et al., 2013) and either Na_2S, K_2S or LiS is the dominant S species in reduced molten salt system, we suggest that differences in bonding energies when comparing the different sulfide species are most likely responsible for possible variation in $\alpha(SO_4^{2-}_{melt} - S^{2-}_{melt})$ with changing composition from silicate to salt melt. Hence, as a first approximation, the *T* dependence determined by the authors for $\alpha(SO_4^{2-}_{melt} - H_2S_{gas})$ may be more realistic, considering that the fluid composition is similar to that expected in natural systems (see also Section 5.2).

Sakai et al. (1982) and De Hoog et al. (2001) have shown that the S isotope fractionation between fluid and melt can be described by three fractionation pair: *i)* $\alpha(SO_{2\ gas} - H_2S_{gas})$, *ii)* $\alpha(SO_4^{2-}_{melt} - S^{2-}_{melt})$, and *iii)* $\alpha(H_2S_{gas} - S^{2-}_{melt})$. However, considering the four most important S species in silicate melt and coexisting aqueous fluid ($SO_4^{2-}_{melt}$, S^{2-}_{melt}, $SO_{2\ fluid}$, H_2S_{fluid}; see, e.g., Marini et al., 1998; Burgisser et al., 2008) a model for the evaluation of $\alpha_{g\text{-}m}$ and, thus, of $\Delta^{34}S_{g\text{-}m}$ at *P-T-fO*$_2$ relevant for magmatic systems, may have to include the four predominant S isotope fractionation pairs: *i)* $SO_{2\ (gas)} - SO_4^{2-}_{(melt)}$, *ii)* $H_2S_{gas} - SO_4^{2-}_{melt}$, *iii)* $SO_{2\ gas} - S^{2-}_{melt}$ and *iv)* $H_2S_{gas} - S^{2-}_{melt}$. In the following section we will use the new fractionation data presented in this study to estimate fractionation factors for these pairs. Furthermore, we present an adjusted model based on four fractionation factors and compare the

425 resulting trend with the approach used by Sakai et al. (1982), De Hoog et al. (2001) and others. Here,
426 we will use the same input parameters (i.e., S speciation and $\alpha_{g\text{-}m}$ at given fO_2) to allow comparison.
427
428 Figure 5
429
430 ***5.2 Modeling of the fluid-melt S isotope fractionation***
431 Using our experimental data we developed a new model for the evaluation of $\alpha_{g\text{-}m}$ at given fO_2 and $T \approx$
432 1030°C. A good knowledge of the S speciation in the melt and the coexisting fluid at given P-T-fO_2 is
433 required for the calculations. For our model we estimated the S speciation in the fluid and the melt as
434 follows:
435 *Sulfur speciation in melt:* The fO_2 of each experiment can be utilized to estimate the molar fraction of
436 S dissolved as sulfate in the melt, $x(SO_4^{2-})_{melt}$, using equation 5 provided by Jugo et al. (2010).
437
438 $$x(SO_4^{2-})_{melt} = S^{6+} / \Sigma S = 1 / (1 + 10^{(2.1 - 2 \cdot \Delta QFM)}) \quad (5)$$
439
440 where ΣS is the sum of S dissolved as sulfide (S^{2-}) and sulfate (S^{6+}) in the melt and $x(SO_4^{2-})_{melt} = 1 -$
441 $x(S^{2-})_{melt}$. Notably, equation 5 was calibrated based on XANES measurements at the S K-edge on
442 basaltic glasses and the sulfate-sulfide transition predicted by the equation differs slightly when
443 compared to that in andesitic systems (see below, this Section and Fiege et al., 2014a).
444 *Sulfur speciation in fluid:* The molar H_2S/SO_2 fraction in the gas phase was estimated using the
445 program *DCompress* provided by Alain Burgisser (CNRS, Chambéry, France), which is based on the
446 work of Burgisser et al. (2008) to model the degassing of rhyolitic melts and on data from Lesne et al.
447 (2011a; 2011b) and Lesne (2008) to model the degassing of basaltic melts. The program allows the
448 estimation of the molar H_2S/SO_2 fraction in a S-O-H fluid coexisting with basaltic (at 1000 to 1400°C)
449 or rhyolitic melts (at 710 to 910°C) for a given fO_2. Notably, *DCompress* does not yet cover
450 intermediate melt compositions such as the andesite used in our experiments or $T > 910$°C for rhyolitic
451 systems. However, the program is based on some of the most recent and relevant (high P-T)
452 experimental data and by calculating trends for both, rhyolitic and basaltic systems, we can account for

453 the possible effect of bulk composition on S speciation in the fluid phase. Hence, the decompression
454 (from 300 to 70 MPa) of a rhyolitic (at 900°C) and a basaltic melt (at 1030°C) containing initially 6
455 wt% H_2O, 1000 ppm S and 0.1 wt% gas was simulated for fO_2 ranging from QFM-1 to QFM+5. The
456 modeled molar H_2S/SO_2 fractions in the fluid phases were used to calculate the fraction of SO_2
457 [$x(SO_2)_{fluid}$ = (mol SO_2) / (mol SO_2 + mol H_2S)] and H_2S [$x(H_2S)_{fluid} = 1 - x(SO_2)_{fluid}$] in the fluid phase
458 as a function of fO_2 for a rhyolitic and basaltic composition. The lower *T* applied for the *DCompress*
459 calculations for rhyolitic composition when compared to *T* of our experiments results in a shift of the
460 sulfide-sulfate transition towards higher fO_2; i.e., the rhyolite trend overestimates the H_2S/SO_2 fraction
461 in the fluid phase at intermediate fO_2. However, considering that both, increasing *T* (900 to 1030°C)
462 and changes in melt composition from rhyolite to basalt shift the sulfide-sulfate transition towards
463 lower fO_2, calculating trends for rhyolite at 900°C and for basalt at 1030°C should provide maximum-
464 minimum S speciation data for the studied andesitic system at 1030°C.
465 The main assumptions for the new model are: *a)* The fluid-melt isotope fractionation can be described
466 by $\alpha(SO_{2\ gas} - SO_4^{2-}{}_{melt})$ at very oxidizing conditions and *b)* by $\alpha(H_2S_{\ gas} - S^{2-}{}_{melt})$ at very reducing
467 conditions. The average $\alpha_{g\text{-}m}$ of ~0.9985 derived from experiments conducted under oxidizing
468 conditions ($\log(fO_2/bar)$ > QFM+2.8) is assumed to represent the fractionation pair $SO_{2\ gas} - SO_4^{2-}{}_{melt}$,
469 considering that $x(SO_4^{2-})_{melt}$ and $x(SO_2)_{fluid}$ are nearly 1 at $\log(fO_2/bar)$ > QFM+2.8. Furthermore, an
470 average $\alpha_{g\text{-}m}$ of ~1.0042 was determined for $\log(fO_2/bar) \approx$ QFM+1.1 (experiments RED-1 to RED-4;
471 AHC-3; andesitic composition), corresponding to $x(SO_4^{2-})_{melt}$ and $x(SO_2)_{fluid}$ of ~0.5 if a basaltic melt
472 composition is assumed to model the S speciation [i.e., speciation estimated using *DCompress* and
473 Jugo et al. (2010); see above, this Section]. The $\alpha_{g\text{-}m}$ fractionation factor of ~1.0042, and the
474 determined value for $\alpha(SO_{2\ gas} - SO_4^{2-}{}_{melt})$, are used to estimate a value of $\alpha(H_2S_{\ gas} - S^{2-}{}_{melt})$ for
475 basaltic systems. The same approach can be used to estimate a value of $\alpha(H_2S_{\ gas} - S^{2-}{}_{melt})$ at QFM+1.1
476 for rhyolitic systems if $x(SO_2)_{fluid}$ is modeled using *DCompress* for rhyolite melts. The estimated
477 $\alpha(H_2S_{\ gas} - S^{2-}{}_{melt})$ values are 1.0099 and 1.0050 for basaltic and rhyolitic systems, respectively (Table
478 3). The calculations were repeated using the $S^{6+}/\Sigma S$ ratio estimated from the XANES spectra to
479 account for the observed discrepancies between the prevailing fO_2 in the vessel and $fO_2(XANES)$. In
480 this case, the estimated $\alpha(H_2S_{\ gas} - S^{2-}{}_{melt})$ values are 1.0073 and 1.0046 for basaltic and rhyolitic

systems, respectively (Table 3). The fractionation factor $\alpha(H_2S_{gas} - SO_4^{2-}{}_{melt})$ was estimated using the results of Miyoshi et al. (1984) who used Na_2SO_4 melt and (aqueous) H_2S fluid in their experiments. Subsequently, $\alpha(SO_{2\ gas} - S^{2-}{}_{melt})$ can be calculated using equation 6.

$$\alpha(SO_{2\ gas} - S^{2-}{}_{melt}) = \alpha(SO_{2\ gas} - SO_4^{2-}{}_{melt}) + \alpha(H_2S_{gas} - S^{2-}{}_{melt}) - \alpha(H_2S_{gas} - SO_4^{2-}{}_{melt}) \quad (6)$$

The application of the data of Miyoshi et al. (1984) to extract $\alpha(H_2S_{gas} - SO_4^{2-}{}_{melt})$ for silicate systems may be problematic (see Section 5.1), but can be tested using the *T* dependence of $\alpha(SO_{2\ gas} - H_2S_{gas})$ given by Taylor (1986) based on theoretical calculations of Richet et al. (1977). If the average values derived for $\alpha(H_2S_{gas} - S^{2-}{}_{melt})$ and $\alpha(SO_{2\ gas} - S^{2-}{}_{melt})$ (Table 3) are used to calculate the fractionation between H_2S and SO_2 in a fluid phase, a value of $\alpha(SO_{2\ gas} - H_2S_{gas})$ of 1.0023 is obtained, which is similar to the value calculated using the data in Taylor (1986).

The fluid-melt fractionation factors used for the modeling of the isotopic fractionation are summarized in Table 3. The highest and lowest values determined for $\alpha(H_2S_{gas} - S^{2-}{}_{melt})$ and $\alpha(SO_{2\ gas} - S^{2-}{}_{melt})$ (Table 3) are suggested to represent the maximum and minimum fractionation factors which can be expected for andesitic systems at 1030°C, because the uncertainty of the estimated S speciation at given fO_2 dominates over all other uncertainties; e.g., the analytical error of SIMS, IR and EMP. They were applied to calculate fractionation factors at given fO_2 [$\alpha_{g\text{-}m}(fO_2)$] using the S speciation in the fluid- (estimated using *DCompress*) and melt-phase (estimated using XANES data and the model of Jugo et al., 2010); see Appendix G for details.

Fig. 6 shows the modeled isotopic fractionation trends. All four trends correlate well with the experimental data at oxidizing conditions but differ by about 0.5 log units in fO_2 at intermediate to reducing conditions. The trends calculated for a basaltic melt composition (blue lines) seem to show a better correlation with the measured $\Delta^{34}S$ values when compared to rhyolite trends (red lines). However, the *T* for the calculations in rhyolitic system using *DCompress* is limited to 900°C, and the observed differences between the measured $\Delta^{34}S$ values and the modeled trends may be related to

both, compositional and *T* differences (i.e., differences between those applied for the *DCompress* modeling and those of the conducted experiments).

The differences between the modeled trends and the experimental data can also be explained by a (slight) shift of the sulfide-sulfate transition towards more oxidizing conditions in the studied andesitic system when compared to the basaltic samples used by Jugo et al. (2010) to determine equation 5, which was applied to estimate $x(SO_4^{2-})_{melt}$. In fact, Baker and Moretti (2011) noted that the dependence of $S^{6+}/\Sigma S$ on fO_2 (i.e., the sulfide-sulfate transition) is significantly affected (e.g.) by *T*, *P*, and melt composition. Fig. 4a in Fiege et al. (2014a) indicates that the sulfide-sulfate transition in the studied evolved andesite glasses may be shifted by about +0.5 log units relative to the one for basaltic glasses determined by Jugo et al. (2010). According to the data shown in Fig. 6 the sulfide-sulfate transition in andesite glasses is suggested to be at an fO_2 of about QFM+1.8. This is consistent with a comparison of trends for the S speciation in the fluid and melt phase based on different model approaches (see Fig. H.1, Appendix H). For instance, *DCompress* predicts that the S speciation in aqueous fluids coexisting with rhyolitic melt shifts by +0.5 log units when compared to basaltic systems. Notably, the sulfide-sulfate transition predicted by the general model of Wallace and Carmichael (1992), based on experimental results of Carroll and Rutherford (1988), is around ~QFM+1.5 and, thus, somewhat closer to what we suggest for andesitic systems than found by Jugo et al. (2010) for hydrous basaltic compositions. However, the shape of the Wallace and Carmichael (1992) trend differs significantly from more recent and, presumably, more precise predictions (e.g., Jugo et al., 2005, 2010; Botcharnikov et al., 2011). A clear determination of the sulfide-sulfate transition in andesite glasses is needed to improve our model.

In general, the fluid-melt S isotope fractionation at oxidizing conditions is very well constrained by our data. An extrapolation of the S isotope data presented in Mandeville et al. (2009) for natural samples of the climactic eruption of Mt. Mazama (relevant degassing *T* estimated for the samples range from 840 to 975°C) indicates an $\alpha_{g\text{-}m}$ of about 0.9982 at 1030°C and fairly oxidizing conditions (~QFM+1.7 to QFM+1.9 log units), which is within error of our experimental data for oxidized systems. In contrast, the lack of experimental data at $\log(fO_2/\text{bar}) << \text{QFM+1}$ leads to a large error on the estimation of $\alpha(H_2S_{gas} - S^{2-}_{melt})$. However, considering that equilibrium (S) isotope fractionation

effects refer to the effect of atomic mass on bond energy (e.g., O'Neil, 1986) and assuming that differences in bonding energies of S isotopes in melts are negligible when comparing different silicate melt compositions, the average $\alpha(H_2S_{gas} - S^{2-}_{melt})$ of 1.0067 ± 0.0046 determined on the basis of our data may be applicable to a wide range of reduced magmatic systems at 1030°C.

Our model can be further evaluated by using input parameters (i.e., fractionation factors, S speciation data) identical to those applied in our model for the modeling approach of Sakai et al. (1982) and compare both trends. In Fig.7 a re-calculated trend based on the Sakai et al. (1982) model is plotted for comparison. The resulting trend is identical to our trend, showing that the fluid-melt S isotope fractionation can be modeled with both approaches. However, in our opinion, the modeling approach proposed in this study should be easier to follow because its terms clearly delineate which fractionation pairs are required for the estimation of $\alpha_{g\text{-}m}$ at given fO_2. Furthermore, an additional trend plotted in Fig. 7 and based on our model but shifted by 0.5 log units towards more oxidizing conditions, confirms that the proposed model should reproduce our experimental results closely if S speciation models specially designed for intermediate, andesitic systems were available.

Figure 6 and 7; Table 3

5.3 Equilibrium fractionation: Modeling S isotope composition of volcanic gases

The isotopic composition of volcanic gases released from a melt can be estimated using the equations given by Holloway and Blank (1994) for closed and open system degassing, respectively:

$$\delta^{34}S_{m\text{-}f} \approx \delta^{34}S_{m\text{-}i} - (1 - f) \cdot 10^3 \cdot \ln \alpha_{g\text{-}m} \qquad \textit{closed system degassing} \qquad (7)$$

$$\delta^{34}S_{m\text{-}f} \approx (\delta^{34}S_{m\text{-}i} + 10^3) \cdot (f^{\alpha(g\text{-}m)-1}) - 10^3 \qquad \textit{open system degassing} \qquad (8)$$

where f is the fraction of S remaining in the melt as well as $\delta^{34}S_{m\text{-}i}$ and $\delta^{34}S_{m\text{-}f}$ are the initial and the final isotopic composition in the melt phase, respectively. Subsequently, the isotopic composition of the released fluid phase ($\delta^{34}S_{gas}$) can be determined using equation 3. The equilibrium fractionation

563 factor $\alpha_{g\text{-}m}$ for a given fO_2 can be estimated applying the new model described in Section 5.2 and using
564 the average $\alpha_{g\text{-}m}$ values of the four fractionation pairs listed in Table 3. The derived $\alpha_{g\text{-}m}$ values (listed
565 in the figure captions of Fig. 8) can be used to model the isotopic composition of a released fluid
566 ($\delta^{34}S_{gas}$) upon open and closed system degassing (Fig. 8); here, a $\delta^{34}S_{m\text{-}i}$ of 0 ‰ was assumed for the
567 calculations. Significant differences of ≥ 1 ‰ between the modeled trends for closed system and open
568 system degassing are only observed if 35 to 90% of the S in the melt is released and only in reduced
569 systems. Thus, distinguishing between closed and open system degassing based on the S isotope
570 signature of a volcanic gases only may be quite difficult. Nevertheless, Fig. 8a and 8b indicate that
571 even under intermediate redox conditions (~QFM+1.5) considerable fluid-melt S isotope fractionation
572 should be expected.
573 Most importantly, the data reveal that the first fluid released by degassing may be up to ~1.7 ‰ lighter
574 (oxidized magmas) or up to ~6.7 ‰ heavier (reduced magmas) than the $\delta^{34}S$ of the source magma.
575 Considering that fast decompression combined with open system degassing often occurs during
576 explosive, hazardous volcanic events, a distinct change in $\delta^{34}S_{gas}$ detected in the volcanic gas of
577 reduced systems should be expected prior to, or during the initial phase of the eruption. Moreover,
578 model calculations for open system degassing using equation 8 show that $\delta^{34}S$ of the melt ($\delta^{34}S_{m\text{-}f}$) can
579 decrease by >40 ‰ under reducing conditions and increase by >10 ‰ under oxidizing conditions.
580 Hence, the strong variations in $\delta^{34}S$ observed by Shimizu and Mandeville (2011) for some olivine
581 hosted melt inclusion in subduction zone magmas are probably, in part, related to degassing and not
582 only due to slab-derived fluids, which is in agreement with observations of de Moor et al. (2013)
583
584 Figure 8a and 8b
585
586 ***5.4 Implications for studies of natural systems***
587 The new experimental data presented in this study are of great value for a better interpretation of
588 natural S isotope compositions detected in pumices, scoria and volcanic gases. Ohba et al. (2008), for
589 instance, applied the chemical trap method (using KOH solution) to monitor the volcanic gas signature
590 at Miyakejima (Japan). The authors estimated a $\Delta^{34}S_{gas}$ of about -0.3 to -1.0 for two degassing periods

(2001 to summer 2002; summer 2002 to 2005). Ohba et al. (2008) noted that the fO_2 required to produce the observed fractionation may be about QFM+1.3 to QFM+1.9 and, thus, ~0.5 log units higher than estimated petrologically by Yasuda et al. (2001). Ohba et al. (2008) proposed fluid-melt disequilibrium in terms of fO_2 to explain the observed discrepancies. However, the results of Ohba et al. (2008) rely on calculation procedures of Marini et al. (1998) for the estimation of $\alpha_{g\text{-}m}$ for a given fO_2, fH_2O and T. The Marini et al. (1998) model is comparable to that of De Hoog et al. (2001) and also relies on the equation provided by Miyoshi et al. (1984) for the T dependence of $\alpha(SO_4^{2-}{}_{melt} - S^{2-}{}_{melt})$, which is probably not applicable to magmatic systems (see Section 5.1). Considering the new experimental results presented in this study, the isotopic fractionation determined by Ohba et al. (2008) may be explained by comparable redox conditions as determined by Yasuda et al. (2001). This example shows that our findings need to be considered for the interpretation of magmatic S isotope signature. However, the T dependence still needs to be verified to allow the application to a wide range of magmatic systems.

Furthermore, it has been shown by de Moor et al. (2013) that kinetic S isotope fractionation can play a crucial role in natural magmatic systems and can affect the S isotope signature detected in volcanic gases and ejecta to a significant extent. Notably, the large equilibrium S isotope fractionation that we observed for our reduced experiments when compared to previously published values has to be considered for the calculation of the relative effect of kinetic vs. equilibrium S isotope fractionation in natural systems.

6. CONCLUSION

A new experimental approach was applied to investigate S isotope fractionation between fluid and silicate melt. The obtained results provide, for the first time, constraints on fluid-melt S isotope fractionation at geologically relevant P-T-fO_2 conditions with close to natural fluid-melt compositions. Our data indicate that the instrumental S isotope fractionation of the SIMS as well as the gas-melt S isotope fractionation in natural systems is largely independent of the (initial) S isotope composition of the glass, at least in the studied range of $\delta^{34}S$ = -32‰ to +18‰.

618 The new data show that previous models (e.g., De Hoog et al., 2001) based on experiments using
619 simple melt compositions (e.g., molten salt Na_2SO_4 and Na_2S analogies) and theoretical studies from
620 the 1970s and 1980s (summarized by Taylor, 1986) may significantly underestimate the isotopic
621 fractionation at intermediate to reducing conditions. Our results show that under reducing conditions a
622 S isotope fractionation between aqueous fluid and andesitic melt of ≥ 4 ‰ can be expected at 1030°C.
623 The reason for the observed discrepancies is most likely the very limited data available in the literature
624 on S isotope fractionation, which are probably not fully applicable to magmatic systems. Here, our
625 experimental results show that under intermediate to reducing conditions the S isotope fractionation
626 between aqueous fluid and andesitic melt is about one order of magnitude larger than expected
627 previously.
628 In general, measuring S isotope compositions of volcanic material can be of great importance to
629 investigate degassing processes (e.g., distinguish between open and closed system degassing),
630 understand atmospheric transport processes of volcanic gas-ash-clouds and/or assess the source(s) of
631 volatiles in magmatic systems. The presented data will help to understand and interpret related S
632 isotope signatures and especially isotopic data of reduced systems may need to be re-interpreted. The
633 observed independence of $\alpha_{g\text{-}m}$, on the bulk Cl content indicates that the estimated fractionation factors
634 and trends may be applicable to complex multi-component fluid-melt systems. However, future
635 studies should focus on the influence of melt composition and, most importantly, on the *T* dependence.
636

637 **ACKNOWLEDGEMENTS**

638 This project was supported by the German Science Foundation (BE1720/25-1 to H. Behrens), by the
639 German National Academic Foundation, and by Collaborative Research Grants from the U.S. National
640 Science Foundation (EAR-0838482 to C. W. Mandeville, EAR-0838436 to N. Shimizu, and EAR-
641 0838328 to K. A. Kelley). We acknowledge Don Lindsley, Bruce Watson, Jay Thomas, Antonio
642 Buono, for assistance with synthesis of S standard glasses, and Bruce Taylor, Minoru Kusakabe,
643 Shuhei Ono, and Nicole Keller for assistance with sulfur isotopic analyses of synthesized
644 glasses. Special thanks go to Alain Burgisser for providing the *DCompress* model. We would like to
645 thank J. Göttlicher and R. Steininger for their assistance at the SUL-X beamline of ANKA and O.

Dietrich for sample preparation. We are grateful for the constructive reviews and helpful suggestions of the J.C.M De Hoog, N. Métrich, T. Sisson, J.B. Lowenstern and an anonymous reviewer as well as for the editorial work of P. King.

REFERENCES

Allard P. (1983) The origin of hydrogen, carbon, sulfur, nitrogen and rare gases in volcanic exhalations: Evidence from isotope geochemistry. In *Forecasting Volcanic Events* (ed. H. Tazieff and J.-C.Sabroux). Elsevier. pp. 337-386.

Ayris P. M., Lee A. F., Wilson K., Kueppers U., Dingwell D. B. and Delmelle P. (2013) SO_2 sequestration in large volcanic eruptions: High-temperature scavenging by tephra. *Geochim. Cosmochim. Acta* **110**, 58-69.

Baker D. R. and Moretti R. (2011) Modeling the Solubility of Sulfur in Magmas: A 50-Year Old Geochemical Challenge. *Rev. Mineral. Geochem.* **73**, 167-213.

Behrens H. and Stelling J. (2011) Diffusion and Redox Reactions of Sulfur in Silicate Melts. *Rev. Mineral. Geochem.* **73**, 79-111.

Berndt J., Liebske C., Holtz F., Freise M., Nowak M., Ziegenbein D., Hurkuck W. and Koepke J. (2002) A combined rapid-quench and H_2-membrane setup for internally heated pressure vessels: Description and application for water solubility in basaltic melts. *Am. Mineral.* **87**, 1717-1726.

Botcharnikov R. E., Linnen R. L., Wilke M., Holtz F., Jugo P. J. and Berndt J. (2011) High gold concentrations in sulphide-bearing magma under oxidizing conditions. *Nat. Geosci.* **4**, 112-115.

Burgisser A. and Scaillet B. (2007) Redox evolution of a degassing magma rising to the surface. *Nature* **445**, 194-197.

Burgisser A., Scaillet B. and Harshvardhan (2008) Chemical patterns of erupting silicic magmas and their influence on the amount of degassing during ascent. *J. Geophys. Res.* **113**, B12204, 1-14.

Carroll M. R. and Rutherford M. J. (1988) Sulfur Speciation in Hydrous Experimental Glasses of Varying Oxidation-State - Results from Measured Wavelength Shifts of Sulfur X-Rays. *Am. Mineral.* **73**, 845-849.

Coplen T. B. and Krouse, H. R. (1998) Sulphur isotope data consistency improved. *Nature* **392**, 32-32.

De Hoog J. C. M., Taylor B. E. and van Bergen M. J. (2001) Sulfur isotope systematics of basaltic lavas from Indonesia: implications for the sulfur cycle in subduction zones. *Earth Planet. Sci. Lett.* **189**, 237-252.

de Laeter J. R., Bohlke J. K., De Bièvre P., Hidaka H., Peiser H. S., Rosman K. J. R. and Taylor P. D. P. (2003) Atomic weights of the elements: Review 2000 - (IUPAC technical report). *Pure Appl. Chem.* **75**, 683-800.

de Moor J.M., Fischer T.P., Sharp Z.D., King P.L., Wilke M., Botcharnikov R.E., Cotrell E., Zelenski M., Marty B., Klimm K., Rivard C., Ayalew D., Ramirez C. and Kelley K.A. (2013) Sulfur degassing at Erta Ale (Ethiopia) and Masaya (Nicaragua) volcanoes: Implications for degassing processes and oxygen fugacities of basaltic systems. *Geochem. Geophys. Geosyst.* **14**, 4076-4108.

Ding T., Valkiers S., Kipphardt H., De Bièvre P., Taylor P. D. P., Gonfiantini R. and Krouse R. (2001) Calibrated sulfur isotope abundance ratios of three IAEA sulfur isotope reference materials and V-CDT with a reassessment of the atomic weight of sulfur. *Geochim. Cosmochim. Acta* **65**, 2433-2437.

Faure (1986) *Principles of Isotope Geology*. Wiley. 589 pp.

Fiege A., Behrens H., Holtz F. and Adams F. (2014a) Kinetic vs. thermodynamic control of degassing of H_2O-S±Cl bearing andesitic melts. *Geochim. Cosmochim. Acta* **125**, 241-264.

Fiege A., Cichy S. B. and Holtz F. (2014b) Bubble formation during decompression of andesitic melts. *Am. Mineral., in press*, doi: 10.2138/am.2014.4719.

Gerlach T. M. and Nordlie B. E. (1975) The C-O-H-S gaseous system; Part II, Temperature, atomic composition, and molecular equilibria in volcanic gases. *Am. J. Sci.* **275**, 377-394.

690 Halas S. and Szaran J. (2001) Improved thermal decomposition of sulfates to SO_2 and mass spectrometric
691 determinations of $\delta^{34}S$ of IAEA-SO-5, IAEA-SO-6 and NBS-127 sulfate standards. *Rapid Commun. Mass Sp.*
692 **15**, 1618-1620.

693 Holloway J. R. and Blank J. G. (1994). Application of Experimental Results to C-O-H Species in Natural Melts.
694 *Rev. Mineral.* **30**, 187-230.

695 Hut G. (1987) *Consultants' Group Meeting on Stable Isotope Reference Samples for Geochemical and*
696 *Hydrological investigations*, Report to the Director General, International Atomic Energy Agency, Vienna, pp.
697 42.

698 Jugo P. J., Luth R. W. and Richards J. P. (2005) Experimental data on the speciation of sulfur as a function of
699 oxygen fugacity in basaltic melts. *Geochim. Cosmochim. Acta* **69**, 497-503.

700 Jugo P. J., Wilke M. and Botcharnikov R. E. (2010) Sulfur K-edge XANES analysis of natural and synthetic
701 basaltic glasses: Implications for S speciation and S content as function of oxygen fugacity. *Geochim.*
702 *Cosmochim. Acta* **74**, 5926-5938.

703 Katsura T. and Nagashima S. (1974) Solubility of Sulfur in Some Magmas at 1-Atmosphere. *Geochim.*
704 *Cosmochim. Acta* **38**, 517-531.

705 Keppler H. (1999) Experimental evidence for the source of excess sulfur in explosive volcanic eruptions. *Science*
706 **284**, 1652-1654.

707 Keppler H. (2010) The distribution of sulfur between haplogranitic melts and aqueous fluids. *Geochim.*
708 *Cosmochim. Acta* **74**, 645-660.

709 Klimm K., Kohn S. C., Botcharnikov R. E. (2012) The dissolution mechanism of sulphur in hydrous silicate
710 melts. II: Solubility and speciation of sulphur in hydrous silicate melts as a function of fO_2. *Chem Geol.* **322-323**,
711 250-267.

712 Labidi J., Cartigny P., Birck J.L., Assayag N. and Bourrand J.J. (2012) Determination of multiple sulfur isotopes
713 in glasses: A reappraisal of the MORB $\delta^{34}S$. *Chem. Geol.* **334**, 189-198.

714 Lesne P. (2008) Etude expérimentale de la solubilité des volatils C-H-O-S dans les basaltes alcalins italiens :
715 simulations numériques du dégazage chimique : application à l'Etna. Ph. D. thesis, Université d'Orléans

716 Lesne P., Scaillet B., Pichavant M. and Beny J.-M. (2011a) The carbon dioxide solubility in alkali basalts: an
717 experimental study. *Contrib. Mineral. Petrol.* **162**, 153-168.

718 Lesne P., Scaillet B., Pichavant M. and Beny J.-M. (2011b) The H_2O solubility in alkali basaltic melts: an
719 experimental study. *Contrib. Mineral. Petrol.* **162**, 133-151.

720 Mandeville C. W. (2010) Sulfur: A Ubiquitous and Useful Tracer in Earth and Planetary Sciences. *Elements* **6**,
721 75-80.

722 Mandeville C. W., Shimizu N., Kelley K. A. and Cheek L. (2008) Sulfur Isotope Variation in Basaltic Melt
723 Inclusions from Krakatau Revealed by a Newly Developed Secondary Ion Mass Spectrometry Technique for
724 Silicate Glasses. *EOS Trans. AGU* **83**(53), Fall Meet. Suppl., San Fransisco, Abstract V13-F07.

725 Mandeville C. W., Shimizu N., Kelley K. A. and Metrich N. (2010) Sulfur isotope variation in arc basalts
726 revealed by secondary ionization mass spectrometry: Measurements of melt inclusions. *Geochim. Cosmochim.*
727 *Acta* **74**(11), Goldschmidt Meet. 2010 Suppl., Knoxville, Tennessee, A663.

728 Mandeville C. W., Webster J. D., Tappen C., Taylor B. E., Timbal A., Sasaki A., Hauri E., Bacon C. R. (2009)
729 Stable isotope and petrologic evidence for open-system degassing during the climactic and pre-climactic
730 eruptions of Mt. Mazama, Crater Lake, Oregon. *Geochim. Cosmochim. Acta* **73**, 2978-3012.

731 Marini L., Chiappini V., Cioni R., Cortecci G., Dinelli E., Principe C. and Ferrara G. (1998) Effect of degassing
732 on sulfur contents and $\delta^{34}S$ values in Somma-Vesuvius magmas. *Bull. Volcanol.* **60**, 187-194.

733 Metrich N. and Mandeville C. W. (2010) Sulfur in Magmas. *Elements* **6**, 81-86.

734 Miyoshi T., Sakai H. and Chiba H. (1984) Experimental-Study of Sulfur Isotope Fractionation Factors between
735 Sulfate and Sulfide in High-Temperature Melts. *Geochem. J.* **18**, 75-84.

736 Moretti R. and Ottonello G. (2005) Solubility and speciation of sulfur in silicate melts: The Conjugated Toop-
737 Samis-Flood-Grjotheim (CTSFG) model. *Geochim. Cosmochim. Acta* **69**, 801-823.

738 Moretti R., Papale P. and Ottonello G. (2003) A model for the saturation of C-O-H-S fluids in silicate melts. In
739 *Volcanic Degassing*, Special Publication 213 (ed. C. Oppenheimer et al.). Geological Society of London. pp. 81-
740 101.

741 Müller-Simon H. (2011) Fining of Glass Melts. *Rev. Mineral. Geochem.* **73**, 337-361.

742 Nagashima S. and Katsura T. (1973) Solubility of Sulfur in Na_2O-SiO_2 Melts under Various Oxygen Partial
743 Pressures at 1100 °C, 1250 °C, and 1300 °C. *B. Chem. Soc. Jpn.* **46**, 3099-3103.

744 Nemec L. (1980a) The behavior of bubbles in glass melts. Part 1. Bubble size controlled by diffusion. *Glass*
745 *Technol.* **21**, 134-138.

746 Nemec L. (1980b) The behavior of bubbles in glass melts. Part 2. Bubble size controlled by diffusion and
747 chemical reaction. *Glass Technol.* **21**, 139-144.

748 O'Neil J. R. (1986) Theoretical and experimental aspects of isotopic fractionation. *Rev. Mineral. Geochem.* **16**,
749 1-40.

750 Ohba T., Nogami K., Hirabayashi J.-I. and Mori T. (2008) Isotopic fractionation of SO_2 and H_2S gases during
751 the absorption by KOH solution, with the application to volcanic gas monitoring at Miyakejima Island, Japan.
752 *Geochem. J.* **42**, 119-131.

753 Ohmoto H. and Lasaga A. C. (1982) Kinetics of reactions between aqueous sulfates and sulfides in hydrothermal
754 systems. *Geochim. Cosmochim. Acta* **46**, 1727-1745.

755 Ohmoto H. and Rye R. O. (1979) Isotopes of sulfur and carbon. In *Geochemistry of Hydrothermal Ore Deposits*
756 (ed. H. L. Barnes), Wiley. pp. 509-567.

757 Richet P., Bottinga Y. and Janoy M. (1977) A review of hydrogen, carbon, nitrogen, oxygen, sulphur, and
758 chlorine stable isotope enrichment among gaseous molecules. *Annu. Rev. Earth Planet. Sci.* **5**, 65-110.

759 Sakai H., Casadevall T. J. and Moore J. G. (1982). Chemistry and isotope ratios of sulfur in basalts and volcanic
760 gases at Kilauea volcano, Hawaii. *Geochim. Cosmochim. Acta* **46**, 729-738.

761 Sasaki A., Arikawa Y. and Folinsbee R. E. (1979) Kiba reagent method of sulfur extraction applied to isotopic
762 work. *Bull. Geol. Surv. Jpn.* **30**, 241-245.

763 Schuessler J. A., Botcharnikov R. E., Behrens H., Misiti V. and Freda C. (2008) Oxidation state of iron in
764 hydrous phono-tephritic melts. *Am. Mineral.* **93**, 1493-1504.

765 Schwab R. G. and Küstner D. (1981) The equilibrium fugacities of important oxygen buffers in technology and
766 petrology. *Neues Jahrbuch Mineral.* **140**, 112–142.

767 Shimizu N. and Mandeville C. W. (2011) A sulfur isotope perspective of fluid transport across subduction zones.
768 Abstract V53F-08 presented at 2011 Fall Meeting, AGU, San Francisco, Calif., 5-9 Dec.

769 Sparks R.S.J., Barclay J., Jaupart C., Mader H.M. and Phillips J.C. (1994) Physical Aspects of Magma
770 Degassing – I. Experimental and theoretical constraints on vesiculation. *Rev. Mineral.* **30**, 413-455.

771 Taylor B. E. (1986). Magmatic Volatiles - Isotopic Variation of C, H, and S. *Rev. Mineral.* **16**, 185-225.

772 Ueda A. and Sakai H. (1984) Sulfur isotope study of Quaternary volcanic rocks from the Japanese Islands Arc.
773 *Geochim. Cosmochim. Acta* **48**, 1837-1848.

774 Wallace P. and Carmichael I. S. E. (1992) Sulfur in Basaltic Magmas. *Geochim. Cosmochim. Acta* **56**, 1863-
775 1874.

776 Webster J. D. and Botcharnikov R. E. (2011) Distribution of Sulfur Between Melt and Fluid in S-O-H-C-Cl-
777 Bearing Magmatic Systems at Shallow Crustal Pressures and Temperatures. *Rev. Mineral. Geochem.* **73**, 247-
778 283.

779 Wilke M., Behrens H., Burkhard D. J. M. and Rossano S. (2002) The oxidation state of iron in silicic melt at 500
780 MPa water pressure. *Chem. Geol.* **189**, 55-67.

781 Wilke M., Klimm K. and Kohn S. C. (2011) Spectroscopic Studies on Sulfur Speciation in Synthetic and Natural
782 Glasses. *Rev. Mineral. Geochem.* **73**, 41-78.

783 Yasuda A., Nakada S. and Fujii T. (2001) Sulfur Abundance and Redox State of Melt Inclusions from Miyake-
784 jima 2000 Eruption Products. *Bull. Volcanol. Soc. Jpn.* **46**, 165-173.

Zajacz Z., Candela P. A., Piccoli P. M. and Sanchez-Valle C. (2012) The partitioning of sulfur and chlorine between andesite melts and magmatic volatiles and the exchange coefficients of major cations. *Geochim. Cosmochim. Acta* **89**, 81-101.

Zajacz Z., Candela P. A., Piccoli P. M., Sanchez-Valle C. and Wälle M. (2013) Solubility and partitioning behavior of Au, Cu, Ag and reduced S in magmas. *Geochim. Cosmochim. Acta* **112**, 288-304.

FIGURE CAPTIONS

Fig. 1: S isotopic composition ($\delta^{34}S_{melt}$) of selected experimental series conducted under oxidizing conditions ($\log(fO_2/\text{bar}) > \text{QFM}+2.7$) plotted against fraction of S remaining in the melt phase (*f*). The initial $\delta^{34}S_{melt}$ (0% S degassed; $f = 1.0$) was 20.03 ± 2.11 (AH), 0.93 ± 0.86 (GYC) or -32.22 ± 0.16 (SD1), respectively.

(a) AH data have to be interpreted with caution due to the large isotopic variation detected in the AH starting glass (see Section 3.2.1).

Fig. 2: Isotopic fractionation of S at various fO_2. The normalized $\delta^{34}S_{melt}$ is plotted against fraction of S remaining in the melt phase (*f*). The figure shows all Cl free experiments except AHC, because of the varying fO_2 within this experimental series.

(a) AH data have to be interpreted with caution due to the large isotopic variation detected in the AH starting glass (see Section 3.2.1).

Fig. 3: Influence of t_A on $\alpha_{g\text{-}m}$ at constant *r* of 0.1 MPa/s.

Fig. 4: S isotope fractionation factor $\alpha_{g\text{-}m}$ plotted against fO_2. For clarity, the typical errors for $\alpha_{g\text{-}m}$ and fO_2 are illustrated by the black cross in the upper right corner. The final *P* of the decompression experiments was typically 70 MPa (see Table 2).

(a) SD1 experiments: quenched at final *P* of 30, 70 or 100 (see Table 2).

Fig. 5: $\Delta^{34}S_{g\text{-}m}$ of all experimental series plotted against fO_2. The displayed trend line was calculated for 1030°C following the approach of de Hoog et al. (2001) and is plotted for comparison. The dotted trend represents an extrapolation of the de Hoog et al. (2001) model.

816 *Note:* Only average $\Delta^{34}S_{g\text{-}m}$ values for each experimental series at a given fO_2 are displayed.

817 Error bars: 1 σ based on the $\Delta^{34}S_{g\text{-}m}$ values determined for each experiment.

818

819 **Fig. 6:** Modeled dependence of $\Delta^{34}S_{g\text{-}m}$ on fO_2 for rhyolitic and basaltic melts at 1030°C. $\Delta^{34}S_{g\text{-}m}$

820 values of all experimental series are plotted for comparison.

821 *Note:* The S speciation in the melt was modeled using equation 5 (Jugo et al., 2010). The S speciation

822 in the fluid was modeled using the program *DCompress* for a rhyolitic system at 900°C and for a

823 basaltic system at 1030°C, respectively; see text for details.

824 Only average $\Delta^{34}S_{g\text{-}m}$ values for each experimental series at a given fO_2 are displayed.

825 Error bars: 1 σ based on the $\Delta^{34}S_{g\text{-}m}$ values determined for each experiment.

826

827 **Fig. 7:** Comparison of the new model with the approach of Sakai et al. (1982).

828 *Note:* The model approach of Sakai et al. (1982) was used by De Hoog et al. (2001).

829 (a) Trend calculated based on the model proposed in this study is shifted by +0.5 log units fO_2 to

830 account for the compositional dependence of the sulfide-sulfate transition in silicate melts and

831 coexisting fluids (see Section 5.2 and Appendix G)

832 (b) Trend predicted following the model of Sakai et al. (1982) and using identical input parameters

833 (i.e., for S speciation and S isotope fractionation factors) as applied for the "new model" (see Section

834 5.2).

835 Error bars: 1 σ based on the $\Delta^{34}S_{g\text{-}m}$ values determined for each experiment.

836

837 **Fig. 8a/b:** $\delta^{34}S_{gas}$ plotted against the relative fraction of S degassed from the melt at log(fO_2/bar)

838 ranging from QFM-0.5 to QFM+3.2. **a)** Closed system degassing. **b)** Open system degassing.

839 The $\alpha_{g\text{-}m}$ values for given fO_2 were estimated using our model for the dependence of $\alpha_{g\text{-}m}$ on fO_2.

840 ($\alpha_{g\text{-}m}$ = 1.0067 for QFM-0.5; 1.0045 for QFM+0.8; 0.9988 for QFM+1.5; 0.9983 for QFM+1.8 and

841 0.9985 for QFM+3.2)

842

843

Table 1: Composition of the anhydrous dacitic andesite glass and the volatile-bearing starting glasses determined by electron microprobe and IR spectroscopy (H_2O).

[wt%]	SiO_2	TiO_2	Al_2O_3	FeO	MnO	MgO	CaO	Na_2O	K_2O	H_2O	SO_3	Cl	Total
Anhydrous	64.79	1.28	15.62	4.94	0.23	1.40	4.92	3.92	1.80	-	-	-	98.91
andesite	*0.59*	*0.07*	*0.22*	*0.33*	*0.04*	*0.06*	*0.20*	*0.25*	*0.07*	-	-	-	*0.78*
AH (a)	61.23	0.85	14.69	4.52	0.21	1.34	4.80	3.69	1.69	6.61	0.32	-	99.90
	0.63	*0.04*	*0.08*	*0.28*	*0.09*	*0.08*	*0.15*	*0.28*	*0.10*	*0.03*	*0.01*	-	*0.81*
GYC	60.75	0.80	14.49	4.45	0.26	1.35	4.77	3.65	1.70	6.50	0.34	-	99.06
	0.42	*0.05*	*0.19*	*0.32*	*0.06*	*0.08*	*0.16*	*0.17*	*0.08*	*0.37*	*0.02*	-	*0.47*
AHC	59.24	0.78	14.09	4.53	0.28	1.26	5.02	3.55	1.66	7.95	0.68	-	99.03
	0.40	*0.06*	*0.20*	*0.26*	*0.10*	*0.10*	*0.25*	*0.15*	*0.05*	*0.48*	*0.02*	-	*0.75*
SD1	60.91	0.81	14.57	4.65	0.22	1.34	4.41	3.49	1.66	5.79	0.31	-	98.39
	0.84	*0.02*	*0.14*	*0.11*	*0.06*	*0.07*	*0.04*	*0.25*	*0.04*	*0.48*	*0.02*	-	*1.06*
GYB	61.11	0.82	14.67	4.43	0.27	1.23	4.91	3.56	1.68	6.33	0.36	-	99.36
	0.48	*0.04*	*0.22*	*0.39*	*0.08*	*0.18*	*0.20*	*0.27*	*0.17*	*0.79*	*0.02*	-	*0.77*
SD2	61.94	0.82	15.30	4.48	0.20	1.34	4.71	3.62	1.70	4.55	0.29	-	99.19
	0.36	*0.02*	*0.15*	*0.14*	*0.03*	*0.08*	*0.09*	*0.16*	*0.03*	*0.09*	*<0.01*	-	*0.44*
GYClA	60.63	0.82	14.98	4.12	0.19	1.32	4.48	3.73	1.67	6.56	0.25	0.10	98.84
	0.29	*0.03*	*0.27*	*0.17*	*0.03*	*0.06*	*0.06*	*0.28*	*0.03*	*0.24*	*0.05*	*<0.01*	*1.33*
GYMClA (a)	60.65	0.83	14.92	4.33	0.17	1.41	5.19	3.43	1.65	6.29	0.67	0.05	99.59
	0.34	*0.02*	*0.18*	*0.07*	*0.02*	*0.03*	*0.06*	*0.26*	*0.03*	*0.24*	*<0.01*	*<0.01*	*0.49*
RED	60.76	0.95	14.91	4.50	0.24	1.41	5.00	3.71	1.72	6.71	1623	-	100.32
	0.55	*0.06*	*0.26*	*0.31*	*0.02*	*0.10*	*0.28*	*0.19*	*0.10*	*0.18*	*242*	-	*0.35*
QFMClA (a)	60.83	0.79	14.92	4.63	0.15	1.33	4.47	4.05	1.57	6.58	0.07	0.10	99.50
	0.43	*0.03*	*0.15*	*0.12*	*0.07*	*0.03*	*0.05*	*0.23*	*0.02*	*0.13*	*<0.01*	*<0.01*	*0.42*

Notes: Error in *italic*:1 σ standard deviations based on microprobe analysis; number of EMP analyses: 15 to 20; (a) compositions provided by Fiege et al. (2014).

844

Table 2. Experimental results. All synthesizes and experiments were conducted in IHPVs at 1030 ± 10 °C.

Sample ID	p_S [MPa]	t_I [min]	r [MPa/s]	p_E [MPa]	t_A [min]	ΔQFM	$S^{6+}/\Sigma S$	H_2O [wt%]	Cl [wt%]	S [ppm]	%S degass.	$\delta^{34}S_{melt}$ [‰]	$\delta^{34}S_{fluid}$ [‰]	$\alpha_{g\text{-}m}$	n (SIMS)	Comments
AH (a)	500	xx	xx	500	o. n.	3.7 (b)	nd	6.61 ± 0.03	xx	1266 ± 140	xx	20.03 ± 2.11	xx	xx	5	xx
AH-3 (a)	500	60	0.16	71	1083	4.2 (b)	>0.80	3.56 ± 0.05	xx	720 ± 236	43 ± 5	22.38 ± 0.85	16.93	0.9946	6	xx
AH-4 (a)	500	60	0.17	71	d. r. q.	4.2 (b)	nd	3.97 ± 0.29	xx	130 ± 50	90 ± 14	23.03 ± 2.27	19.69	0.9967	5	NQ
GYC	500	xx	xx	500	o. n.	3.7 (b)	*1.03*	6.50 ± 0.37	xx	1376 ± 60	xx	0.94 ± 0.93	xx	xx	5	xx
GYC-1	505	40	0.09	65	60	4.2 (b)	>0.74	2.49 ± 0.07	xx	380 ± 85	72 ± 4	2.42 ± 1.66	0.37	0.9980	3	xx
GYC-2	505	5	0.16	71	d. r. q.	4.2 (b)	nd	3.64 ± 0.07	xx	375 ± 100	73 ± 5	1.75 ± 0.75	0.63	0.9989	5	xx
GYC-3	402	5	0.05	70	d. r. q.	4.2 (b)	nd	3.34 ± 0.07	xx	636 ± 116	54 ± 2	1.76 ± 0.67	0.22	0.9985	3	xx
AH-C	450	xx	xx	450	o. n.	3.9 (b)	0.98	7.95 ± 0.48	xx	2703 ± 65	xx	23.21 ± 0.27	xx	xx	5	xx
AHC-1	450	40	0.08	71	120	4.2 (b)	>0.89	3.58 ± 0.05	xx	916 ± 50	66 ± 1	24.27 ± 0.64	22.67	0.9984	3	xx
AHC-3	414	40	0.08	73	900	1.2 (c)	>0.52	3.60 ± 0.06	xx	315 ± 80	88 ± 6	22.84 ± 0.56	23.26	1.0004	3	xx
AHC-4	403	5	0.02	71	d. r. q.	4.2 (b)	nd	3.60 ± 0.08	xx	1190 ± 27	56 ± 1	23.72 ± 2.09	22.82	0.9991	5	xx
SD1	502	xx	xx	502	o. n.	3.6 (b)	>0.85	5.79 ± 0.48	xx	1223 ± 71	xx	-32.22 ± 0.16	xx	xx	3	xx
SD1-300	405	5	0.10	34	d. r. q.	2.8	nd	2.02 ± 0.15	xx	146 ± 64	88 ± 17	-30.93 ± 0.42	-32.39	0.9985	2	xx
SD1-700	410	5	0.10	70	d. r. q.	3.2	(>0.66)	3.90 ± 0.15	xx	170 ± 35	86 ± 4	-30.84 ± 0.19	-32.44	0.9984	2	xx
SD1-1000	389	5	0.10	100	d. r. q.	3.4	(>0.67)	4.97 ± 0.35	xx	274 ± 62	78 ± 4	-31.00 ± 2.01	-32.57	0.9984	3	xx
GYB	500	xx	xx	500	o. n.	3.6 (b)	0.98	6.33 ± 0.79	xx	1451 ± 70	xx	3.38 ± 0.25	xx	xx	3	xx
GYB-1	420	60	0.07	74	1087	1.2	0.71	3.08 ± 0.09	xx	405 ± 95	72 ± 4	2.91 ± 0.68	3.57	1.0007	3	xx
GYB-3	420	60	0.07	74	1087	1.7	(0.47)	3.78 ± 0.06	xx	260 ± 70	82 ± 6	3.70 ± 0.56	3.32	0.9996	2	xx
SD2	500	xx	xx	500	o. n.	3.3 (b)	nd	4.55 ± 0.09	xx	1167 ± 20	xx	-16.58 ± 1.03	xx	xx	3	xx
SD2-1	410	5	0.10	70	d. r. q.	2.1	0.96	3.82 ± 0.28	xx	329 ± 86	72 ± 5	-20.0 ± 2.4 (d)	-15.25	1.0048	1	xx
SD2-3	404	5	0.02	70	d. r. q.	1.0	nd	3.74 ± 0.09	xx	202 ± 38	83 ± 3	-19.66 ± 1.10	-15.94	1.0037	4	xx
SD2-5b	405	5	0.10	71	60	1.8	(0.22)	3.46 ± 0.39	xx	190 ± 35	84 ± 3	-18.52 ± 2.21	-16.21	1.0023	2	xx
SD2-6	405	5	0.10	70	300	1.6	(0.57)	3.52 ± 0.13	xx	175 ± 20	85 ± 1	-19.29 ± 0.15	-16.11	1.0032	2	xx
GYClA	508	xx	xx	502	o. n.	0.7	0.09	6.56 ± 0.24	0.103 ± 0.002	1018 ± 188	xx	*7.9 ± 0.7*(e)	xx	xx	*1(+2)*(e)	re-melted (f)
GYClA-1	412	5	0.10	70	d. r. q.	1.7	(0.37)	3.73 ± 0.06	0.089 ± 0.009	184 ± 60	82 ± 12	6.05 ± 0.69	8.32	1.0023	2	xx
GYClA-2	404	5	0.10	70	66	1.9	(0.47)	3.56 ± 0.28	0.081 ± 0.007	148 ± 60	85 ± 17	7.08 ± 1.20	8.05	1.0010	3	NQ
GYClA-3	407	5	0.10	70	300	1.8	(0.29)	3.61 ± 0.07	0.073 ± 0.010	112 ± 52	89 ± 22	5.24 ± 0.48	8.24	1.0030	3	xx
GYClA-4	415	5	0.10	70	4323.5	1.8	(0.35)	1.98 ± 0.03	0.073 ± 0.009	92 ± 48	91 ± 28	4.63 ± 0.28	8.24	1.0036	2	xx

Table 2. Experimental results. *Continuation*

Sample ID	p_S [MPa]	t_I [min]	r [MPa/s]	p_E [MPa]	t_A [min]	ΔQFM	$S^{6+}/\Sigma S$	H_2O [wt%]	Cl [wt%]	S [ppm]	%S degass.	$\delta^{34}S_{melt}$	$\delta^{34}S_{fluid}$	$\alpha_{g\text{-}m}$	n (SIMS)	Comments
GYMClA	495	xx	xx	478	o. n.	0.8	0.23	6.29 ± 0.24	0.051 ± 0.001	1043 ± 143	xx	5.09 ± 1.57	xx	xx	6	re-melted (f)
GYMClA-1	412	5	0.10	70	d. r. q.	1.7	0.33	3.64 ± 0.07	0.047 ± 0.008	356 ± 112	66 ± 8	6.77 ± 1.02	4.22	0.9975	5	xx
GYMClA-3	407	5	0.10	70	300	1.8	(0.65)	3.62 ± 0.06	0.044 ± 0.006	128 ± 36	88 ± 9	5.53 ± 1.24	5.03	0.9995	3	xx
GYMClA-4	415	5	0.10	70	4323.5	1.8	(0.25)	3.61 ± 0.06	0.046 ± 0.006	108 ± 48	90 ± 19	5.41 ± 0.89	5.05	0.9996	5	xx
GYMClA-5	401	5	0.10	71	63	1.9	(0.25)	3.59 ± 0.06	0.045 ± 0.008	176 ± 44	83 ± 7	6.85 ± 1.26	4.73	0.9979	5	xx
RED	495	xx	xx	495	o. n.	0.1	0.03	6.71 ± 0.18	xx	1623 ± 242	xx	7.79 ± 0.20	xx	xx	5	re-melted (f)
RED-1	402	5	0.10	70	60	1.0	(0.33)	3.77 ± 0.09	xx	172 ± 56	89 ± 11	3.25 ± 1.49	8.33	1.0051	3	xx
RED-2	413	5	0.10	71	d. r. q.	1.2	(0.30)	3.45 ± 0.10	xx	284 ± 116	82 ± 16	2.65 ± 1.56	8.88	1.0063	3	xx
RED-3	412	5	0.10	70	300	1.1	(0.25)	3.56 ± 0.06	xx	200 ± 56	88 ± 9	2.69 ± 0.36	8.51	1.0058	3	xx
RED-4	405	5	0.10	70	1204.5	1.1	0.46	3.39 ± 0.41	xx	330 ± 25	80 ± 2	5.11 ± 0.80	8.48	1.0034	4	NQ
QFMClA	508	xx	xx	509	6 days	0.4	(0.04)	6.58 ± 0.13	0.104 ± 0.002	260 ± 19	xx	4.60 ± 1.42	xx	xx	5	xx
QFMClA-3	424	5	0.02	70	d. r. q.	0.8	(0.28)	3.48 ± 0.10	0.095 ± 0.002	52 ± 16	80 ± 8	2.04 ± 0.73	5.25	1.0032	3	xx
QFMClA-4	412	5	0.01	70	d. r. q.	0.9	(0.23)	3.57 ± 0.06	0.097 ± 0.003	69 ± 15	74 ± 4	3.37 ± 0.33	5.04	1.0017	2	xx

Notes: EMP (e.g., S, Cl contents), IR (H_2O contents) and XANES ($S^{6+}/\Sigma S$ ratio) data have been published previously by Fiege et al. (2014a).

Sample ID: starting glasses are written in *italic* – (a) these data have to be interpreted with caution, see Section 3.2.1 for details; p_S*:* start pressure; t_I*:* initial annealing time before decompression; *r:* decompression rate – relative error of the decompression rate ≤7% ; p_E: final pressure after decompression / before rapid quench; t_A*:* annealing time at final *p-T* conditions; Δ*QFM:* Nominal oxygen fugacity determined using the *Shaw*-membrane technique or (b) intrinsic redox conditions determined by, e.g., Berndt et al. (2002) – (c) experiments without *Shaw*-membrane, fO_2 calculated using the initially loaded H_2 pressure; $S^{6+}/\Sigma S$: error probably > 0.1, values in parenthesis refer to samples with very low sulfur content in the melt (< 300 ppm) leading to (very) noisy XANES spectra – *italic* font indicates that the $S^{6+}/\Sigma S$ ratios should be equal to 1, see Fiege et al. (2014a) for details; %*S degass.*: relative fraction of sulfur degassed from the melt upon decompression – determined by mass balance calculations. $\delta^{34}S_{melt}$*:* SIMS data [‰, V-CDT], 1 σ calculated based on the SIMS analyses performed on each sample is given as error – (d) only one spot measured because the sample is highly vesiculated, 2 σ of the 50 analytical cycles is given as error, see Section 3.2.1 – (e) two of the three SIMS measurements show varying count rates during the measurement and were not considered; 2 σ of the 50 analytical cycles is given as error, see Section 3.2.1; $\delta^{34}S_{fluid}$*:* estimated by mass balance calculations [‰, V-CDT]; $\alpha_{g\text{-}m}$: average error ±0.0015, based on the analytical precision of the SIMS measurements; *n:* number of SIMS measurements; *Comments:* (f): starting glass contained quench related S-globules and was re-melted for ~1 h at ~1030°C and 500 MPa to improve homogeneity, see Fiege et al. (2014a) for details.
xx: not relevant or 0; o. n.: over night (≥ 16 h); d. r. q.: direct rapid quench; nd: not determined / no measurement conducted; NQ: normal quench, cooling rate ~150°C/min.

Table 3: Estimated fluid-melt S isotope fractionation factors for 1030°C.

Method	$\alpha(SO_{2\ gas} - SO_4^{2-}{}_{melt})$	$\alpha(H_2S_{gas} - S^{2-}{}_{melt})$	$\alpha(SO_{2\ gas} - S^{2-}{}_{melt})$	$\alpha(H_2S_{\ gas} - SO_4^{2-}{}_{melt})$
oxidized experiments	0.9985	-	-	-
basalt / fO_2	-	1.0099	1.0123	-
basalt / XANES	-	1.0073	1.0096	-
rhyolite / fO_2	-	1.0050	1.0073	-
rhyolite / XANES	-	1.0046	1.0070	-
Miyoshi et al. (1984)	-	-	-	0.9962
average (a)	*0.9985± 0.0007*	*1.0067 ± 0.0023*	*1.0090 ± 0.0025*	*0.9962 ± 0.0002*

Notes: oxidized experiments: average $\alpha_{g\text{-}m}$ derived from experiments conducted at log(fO_2/bar) > QFM+2.8
basalt / fO_2: used basaltic melt composition for the *DCompress* calculations and the nominal fO_2 (Table 2)
basalt / XANES: used basaltic melt composition for the *DCompress* calculations and the XANES data (Table 2)
rhyolite / fO_2: used rhyolitic melt composition for the *DCompress* calculations and the nominal fO_2 (Table 2)
rhyolite / XANES: used rhyolitic melt composition for the *DCompress* calculations and the XANES data (Table 2)
Miyoshi et al. (1984): $10^3 \ln \alpha(SO_4^{2-}{}_{melt} - H_2S_{\ gas}) = (6.5 \pm 0.3) \cdot (10^6 / T^2)$
(a) 1 sigma errors or error calculated based on the uncertainty given by Miyoshi et al. (1984; $\alpha(SO_4^{2-}{}_{melt} - H_2S_{\ gas})$).

APPENDIX

A. Electron microprobe analyses

The major element compositions of all glass samples were determined using a Cameca SX-100 electron microprobe (EMP; acceleration voltage: 15 keV – beam size: 20 µm). The applied beam current was 5 nA (Na) and 10 nA (Si, Ti, Al, Fe, Mn, Mg, Ca, K) and the counting times ranged from 4 s (Na) up to 10 s or 30 s for all major constituents (Si, Ti, Al, Fe, Mn, Mg, Ca, K). Beam current and the counting times were increased for the analyses of S (35 or 100 nA; 240 s) and Cl (35 nA; 120 s) to decrease the detection limit and to improve the counting statistics, respectively (detection limits: ~32 ppm S; ~50 ppm Cl). NIST (U. S. National Institute of Standards and Technology) standards 610 and 620 where measured before and after most analyses to constrain the precision of the measurements.

B. IR spectroscopy

Near infra-red spectroscopy was conducted to determine the water contents in the glass samples. The spectra were collected using a microscope Bruker IRscope II connected to a FTIR spectrometer Bruker IFS 88 equipped with Mercury-Cadmium-Tellurium narrow range detector, a tungsten lamp and a KBr beamsplitter. The spectral resolution was set to 4 cm^{-1} and two to five measurements were collected on each sample.

The measurement of the water content dissolved in glass samples as OH^- groups and molecular H_2O is based on the Beer-Lambert law. Doubly polished glass chips with a thickness of ~120 to ~300 µm, depending on the transmittance of the samples, were prepared for the analysis. The thickness was determined using a conventional micrometer (precision: 3 µm). The absorbances of the IR active bands of molecular water (5200 cm^{-1}) and hydroxyl groups (4500 cm^{-1}) were used for the estimations. The tangential baseline correction described by Ohlhorst et al. (2001) was applied to determine the heights of the H_2O and OH^- bands. The densities of the glasses were calculated following the method of Mandeville et al. (2002) using the known glass composition and the Gladstone-Dale rule (e.g., Silver et al., 1990). The absorption coefficients determined by Fiege et al. (2014) for the andesitic melt composition were applied to quantify the water contents in the glasses [$\varepsilon(5200cm^{-1})$ = 1.27 ± 0.07 L/mol·cm for molecular water; $\varepsilon(4500cm^{-1})$ = 0.84 ± 0.07 L/mol·cm for hydroxyl groups]. A detailed

874 description of the NIR measurements and the determination of the absorption coefficients can be
875 found in Fiege et al. (2014).
876
877 ***C. SIMS calibration***
878 The SIMS measurements were calibrated using a set of natural (JDF46°N, 892-1 MORB glasses) and
879 synthesized silicate glass standards which cover a wide range of melt composition from low (~45
880 wt%) to high SiO_2 (~72 wt%) content (Table C.1). The bulk S isotope compositions of the standard
881 glasses were determined following the KIBA extraction method as described by Sasaki et al. (1979)
882 and Mandeville et al. (1998). For glass JDF 46°N, all Etna glasses (sample ID's beginning with ET,
883 Table C.1) and 892-1 MORB glass, the Ag_2S precipitated and recovered by KIBA extractions was
884 converted to SO_2 gas for measurement of sulfur isotopic ratio by Prof. Minoru Kasakabe (now retired)
885 at Okayama University in Japan according to methods in Sakai et al., (1982). For all other glasses,
886 Ag_2S precipitated after extraction was converted to SF_6 and S isotope analyses were carried out on
887 conventional mass spectrometers (Finnigan MAT 252 or 253). The KIBA extractions and S isotope
888 analyses were conducted by Charles Mandeville and Bruce Taylor at Geological Survey of Canada
889 (GSC) and in the lab of Shuhei Ono at the Massachusetts Institute of Technology (MIT) by Charles
890 Mandeville and Nicole Keller. KIBA extractions with a bulk S yield of $\leq$ 95% were rejected. The
891 average bulk S yield was ~98%. The NIST620 glass and the 892-1MORB glass were analyzed twice
892 and the S isotope compositions were reproduced within ±0.3 to 0.4 ‰. The Results of the bulk S
893 isotope analyses are broken down in Table C.2
894 The major element composition of the glass standards was determined by using EMP analyses
895 following an identical setup as described above (Appendix A). The glasses were analyzed using a
896 Cameca SX100 at the Leibniz Universität Hannover (SD1 and SD2) or at the American Museum of
897 Natural History (all other standards). Notably, the EMP analyses confirmed that all glass standards are
898 chemically homogeneous. The EMP data are listed in Table C.1.
899 Fig. C.1 shows results of the SIMS calibration. Sulfur isotopic compositions obtained by the KIBA
900 extraction ($\delta^{34}S_{true}$) are compared with measured isotopic compositions ($\delta^{34}S_{measured}$). In addition to the
901 KIBA-documented standards, results on two glass starting materials are shown (SD1 and SD2). Their

isotopic compositions ($\delta^{34}S_{true}$) were calculated on the basis of the source of sulfur (IAEA standards SO-6 and NBS 127) used (Section 3.2, main text). The regression line shown in the figure is:

$$\delta^{34}S_{true} = 1.026\ (+0.070, -0.057) \cdot \delta^{34}S_{measured} + 1.840\ (+0.598, -0.503),$$

with $r^2 = 0.992$ and MSWD = 1.033.

It is important to note that the slope of the line is unity (within error) over a large range of sulfur isotopic composition (-31 to +18‰), demonstrating that instrumental mass fractionation encountered here is independent of isotopic composition (purely mass-dependent), and the positive Y-intercept reflects an average instrumental mass fractionation ($\alpha_{measured\text{-}true} = 0.9982 \pm 0.0012$; see Table C.2). The results also show that the major element compositions of glasses do not influence instrumental mass fractionation, as the two high-silica glasses (~72 wt% SiO_2; NIST620, NIST621) are on the same regression line as the silicate glasses with ~44 to ~59 wt% SiO_2. Variations in S speciation in the glasses are not expected to produce a detectable instrumental fractionation, because the energy involved in the sputtered ion formation process (~10-12 keV) is completely overwhelming the bond energies in silicate glasses (typically ~4 eV; e.g., Tichý and Tichá, 1995; Rao, 2002; Dimitrov and Komatsu, 2013). Considering that some glasses are oxidized (e.g., SD1 and SD2: > QFM+3) and some are reduced (e.g., all ET glasses were synthesized in piston cylinder apparatus at 1200°C and 300 MPa using Fe capsules; i.e., buffered at iron-wustite IW << QFM; see Frost, 1991) this is confirmed by the linear trend in Fig. C.1 (see also Table C.2 for available S speciation data). Replicate analyses of one of the MORB glass standards (892-1) reveal an external reproducibility of SIMS analysis with a 2-standard error (n = 13) of ±0.52‰ (see Fig. C.2 and Table C.3).

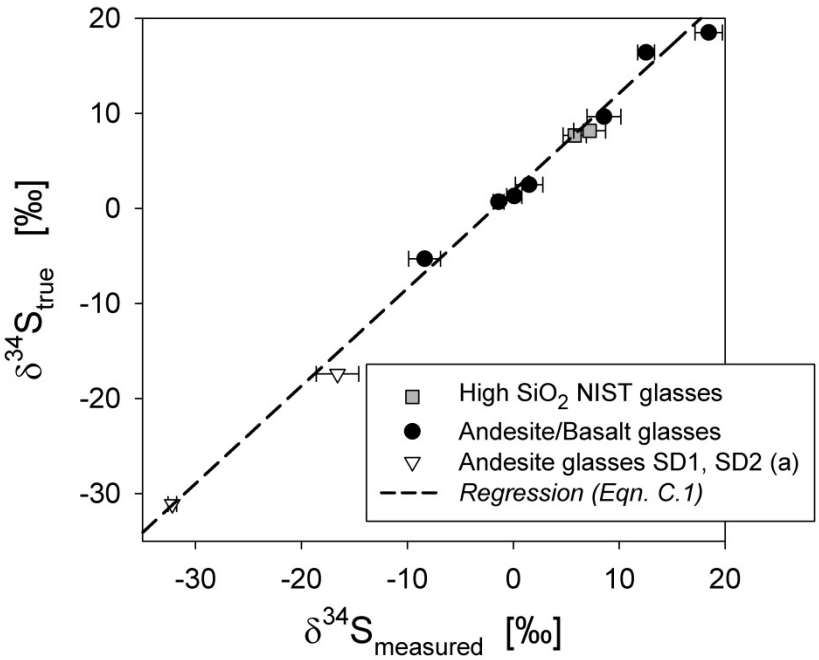

Fig. C.1. SIMS calibration. All 9 silicate glass standard as well as SD1 and SD2 are plotted.
(a) $\delta^{34}S_{true}$ values for SD1 and SD2 are based on the S isotope composition of the IAEA standards used as S source for the glass syntheses (see text).

924

925

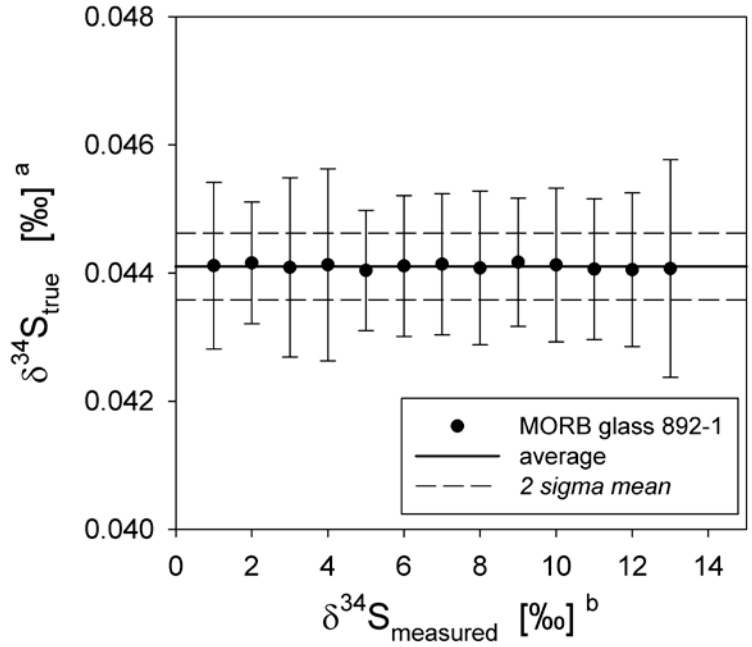

Fig. C.2. High external precision of the SIMS analyses. Replicate analyses of MORB glass 892-1 are displayed (n = 13).

926

Table C.1. Composition of the S isotope glass standards.

sample ID	SiO_2	TiO_2	Al_2O_3	FeO (tot)	MnO	MgO	CaO	Na_2O	K_2O	P_2O_5	S [ppm]	Total
basaltic glasses												
ET83VIIIA	46.37	1.65	18.86	10.64	0.19	5.43	10.19	3.53	1.80	0.44	919	99.33
1 sigma	*0.63*	*0.07*	*0.16*	*0.18*	*0.04*	*0.09*	*0.10*	*0.04*	*0.02*	*0.04*	*49*	
ET83XXA	46.42	1.67	19.39	10.09	0.16	5.44	10.06	3.56	1.78	0.41	822	99.19
1 sigma	*0.37*	*0.07*	*0.13*	*0.20*	*0.03*	*0.07*	*0.11*	*0.04*	*0.03*	*0.06*	*50*	
ET83XVIIIA	48.66	1.55	17.74	9.34	0.18	5.42	10.17	3.59	1.93	n.d.	1025	98.84
1 sigma	*0.12*	*0.18*	*0.49*	*0.61*	*0.09*	*0.21*	*0.13*	*0.06*	*0.37*	*n.d.*	*50*	
ET10B	43.65	1.70	18.78	15.59	0.01	5.49	9.48	3.34	1.87	0.02	839	100.14
1 sigma	*0.53*	*0.07*	*0.20*	*0.69*	*0.02*	*0.11*	*0.17*	*0.06*	*0.04*	*0.02*	*35*	
892-1	51.09	1.78	13.90	12.98	0.23	6.76	10.76	2.50	0.09	0.15	1606	100.64
1 sigma	*0.17*	*0.06*	*0.19*	*0.13*	*0.03*	*0.09*	*0.10*	*0.05*	*0.01*	*0.02*	*38*	
JDF 46°N	50.01	1.97	13.70	12.25	0.21	6.90	10.81	2.64	0.17	0.19	1121	99.13
1 sigma	*0.46*	*0.04*	*0.07*	*0.10*	*0.02*	*0.09*	*0.10*	*0.05*	*0.01*	*0.02*	*65*	
andesitic glass												
Run#144	58.76	0.91	16.68	5.37	0.14	2.55	6.20	3.65	1.37	0.36	1830	96.45
1 sigma	*1.25*	*0.07*	*0.95*	*0.46*	*0.03*	*0.26*	*0.54*	*0.75*	*0.09*	*0.04*	*209*	
NIST glasses (a)												
NIST620 (b)	72.08	0.018	1.80	0.039	n.d.	3.69	7.11	14.39	0.41	n.d.	1121	99.82
uncertainty	*0.08*	*0.002*	*0.03*	*0.004*		*0.05*	*0.05*	*0.06*	*0.03*		80	
NIST621 (c)	71.13	0.014	2.76	0.036	n.d.	0.27	10.71	12.74	2.01	n.d.	521	99.80
uncertainty	*0.03*	*0.003*	*0.04*	*0.003*		*0.03*	*0.05*	*0.05*	*0.03*		80	

The listed glass compositions were determined via EMP analyses (except for the NIST standards). The concentrations are given in wt% (except for S). The compositions of the glasses SD1 and SD2 are given in Table 1 (main text).
n.d.: Not determined; (a) NIST composition as given by the National Institute of Standards and Technology (NIST); (b) GeoReM 1453; G.A. Uriano, http://www.nist.gov/srm/index3column.cfm, NBS[1982] Certificate, NIST SRM 620, soda-lime container glass; contains: 0.056 ± 0.003 wt% As_2O_3; (c) GeoReM 1953; G.A. Uriano, http://www.nist.gov/srm/index3column.cfm, NBS[1982] Certificate, NIST SRM 621, soda-lime flat glass; contains: 0.03 ± 0.001 wt% As_2O_3; 0.12 ± 0.05 wt% BaO; 0.007 ± 0.001 wt% ZrO_2.

927

928

929

930

931

932

933

934

935

936

937

Table C.2. S isotope composition of the glass standards.

sample ID	$\delta^{34}S_{true}$ [‰]	$\delta^{34}S_{measured}$ [‰]	2 sigma mean [‰]	$\alpha_{measured\text{-}true}$	$S^{6+}/\Sigma S$	n
basaltic glasses						
ET83VIIIA	9.65	8.56	1.6	0.9989	~0 (b)	5
ET83XVIIIA	2.49	1.5	1.3	0.9990	~0 (b)	5
ET83XXA	16.4	12.55	0.8	0.9961	~0 (b)	6
ET10B	-5.3	-8.37	1.5	0.9973	~0 (c)	3
892-1	0.7	-1.38	0.52	0.9979	0.06 (d)	13
JDF 46°N	1.3	0.096	0.72	0.9988	-	13
andesitic glass						
Run#144	18.5	18.46	1.3	0.9999	~0 (c)	1 (f)
SD1	-31.1 (a)	-32.2	0.4	-	>0.85 (d)	3
SD2	-17.4 (a)	-16.6	2.0	-	~1 (e)	3
NIST SRM glasses						
NIST620	7.68	5.8	1.1	0.9981	~1 (d)	3
NIST621	8.18	7.21	1.5	0.9990	-	1 (f)

The $\delta^{34}S_{true}$values are based on bulk analyses using KIBA extraction and subsequent mass spectrometry (except for SD1 and SD2). The $\delta^{34}S_{measured}$ values were determined by using *in situ* SIMS analyses.
n: number of analyses; average $\alpha_{true\text{-}measured} = 0.9983 \pm 0.0012$; (a) No KIBA extraction and bulk S isotope analyses were performed. The values for $\delta^{34}S_{true}$ are based on the known S isotope composition of the IAEA standards used as S source for the glasses SD1 and SD2 (see Section 3.2 for details); (b) Equilibrated at $\log(fO_2) <$ QFM using Fe capsules in piston cylinders; (c) Equilibrated at $\log(fO_2) <$ QFM using graphite capsules in piston cylinders; (d) Determined using S XANES; (e) Equilibrated at QFM+3.3 in an IHPV (see Table 2, main text); (f) 2 sigma mean from in-run statistics.

938

Table C.3. Replicate analyses of 892-1 MORB glass demonstrate high external precision of the SIMS analyses.

$^{34}S/^{32}S$ measured (SIMS)	2 sigma mean
0.044115	0.0013
0.044159	0.00095
0.044089	0.0014
0.044129	0.0015
0.04404	0.00094
0.044111	0.0011
0.044137	0.0011
0.04408	0.0012
0.04417	0.001
0.044126	0.0012
0.044061	0.0011
0.044053	0.0012
0.044071	0.0017

Average $^{34}S/^{32}S = 0.044103$; external precision:

±0.52 ‰ (2sigma mean, n = 13)

D. Processing procedure of raw SIMS data

In a first step, the raw SIMS data were time interpolated to account for a drift of the instrumental fractionation during a 50-cycles measurement (as ^{32}S and ^{34}S were alternately detected) and $^{34}S/^{32}S$ ratios were filtered for a 2 sigma deviation. In a second step, the raw $\delta^{34}S$ values were corrected by the long term analytical drift of the instrumental fractionation, using a time based linear interpolation of all $\delta^{34}S$ values of the standard glasses analyzed within one analytical sequence (*analytical sequences* are subdivided by, e.g., sample exchanges, ion-beam shut down, software reset). The instrumental fractionation can be described by the fractionation factor $\alpha_{(t\text{-}m)}$, calculated using the true (t) $\delta^{34}S_t$ of 0.7 ± 0.5 ‰ of the monitored basaltic glass standard (MORB 892-1) and the measured (m) $\delta^{34}S_m$ values of the standard. The instrumental drift within ~6 days of continuous measurement (≙ only short term interruptions between *analytical sequences*; usually < 2 h) is illustrated in Fig. C.1, showing that $\alpha_{(t\text{-}m)}$ ranges from ~0.9825 to ~1.0044. The figure shows that the instrumental drift can be described by a polynomial function. However, within one *analytical sequence* the applied linear interpolation should be adequate. In a final step, to account for short term variations, the pre-corrected $\delta^{34}S$ values of the standards measured right before and after a set of 2-3 sample measurements were used for a time based correction of the $\delta^{34}S$ values using linear interpolation. Note, this short term variation between two standard measurement (within ~2.5 h) is typically < 0.5‰.

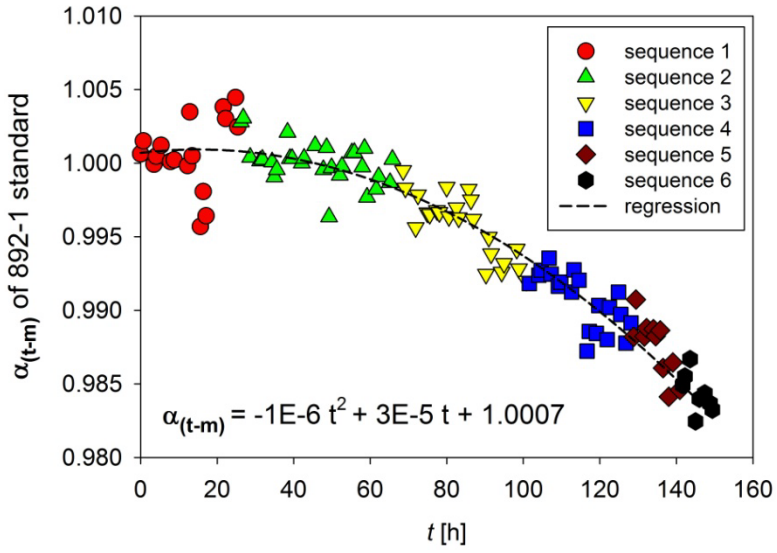

Fig. D.1: Drift of the instrumental fractionation. The different analytical sequences are illustrated by different symbols and color. Mean error for each analysis: ±0.0005 (2 sigma); i.e.,

smaller than symbol size.

E. S speciation: X-ray absorption near edge structure spectroscopy (XANES)

XANES at the S K-edge (2472 eV) was performed on most samples to investigate the S speciation in the andesitic glasses and, if possible, in the quenched fluids, using the SUL-X beamline (uses wiggler as radiation source) at the synchrotron radiation source ANKA (Karlsruhe Institute of Technology, Germany). Noteworthy, the data on S speciation in the glasses have previously been published in Fiege et al. (2014). ANKA operates at a beam energy of 2.5 GeV and a beam intensity of 200 mA. The storage ring has a circumference of 110.4 m. The spectra were collected in fluorescence mode from 2.45 to 2.55 keV. Quick-XAFS scans (XAFS: X-ray absorption fine structure; bragg axis is continuously running) were conducted to avoid irradiation damages (see also Fiege et al., 2014). 5 to 20 spectra were collected on each position, depending on the quality of the single spectrum. The spectra were compared systematically and only spectra showing no evidence for changes in S speciation (e.g., formation of S^{4+}, changes in $S^{6+}/\Sigma S$ ratio), caused by irradiation with the X-ray beam during synchrotron analysis (Wilke et al., 2008), were considered and merged. The energy of the monochromator was calibrated to the white line of sulfate in scotch tape (2481.4 eV).

Two different beam sizes were applied *i)* to evaluate the bulk S speciation in the andesitic glasses (~250×150 µm) and *ii)* to detect small scale variation in S speciation throughout sample (~60×60 µm). These variations can possibly be assigned to S species in the quenched fluid inclusions near the surface (see Appendix Section E).

The energies of the spectra were corrected to the white line of the spectrum of gypsum (2482.84 eV) to be directly comparable to recent studies (e.g., Jugo et al., 2010; Stelling et al., 2011). The XANES spectra collected with the beam size 250×150 µm were used to estimate the fO_2*(XANES)* of the experiments following the approach of Jugo et al. (2010). However, in contrast to Jugo et al. (2010), we applied the fit parameters for andesitic glass compositions determined by Max Wilke (pers. comm.) and used by Botcharnikov et al. (2011), to account for compositional influences.

F. Measuring the S speciation in the quenched fluid

The determination of S species within bubbles using XANES is difficult because the emitted fluorescence decreases exponentially with depth below sample surface. However, the spectra may provide a rough estimation of the prevailing S-speciation in the fluid.

The comparison of spectra collected on sample volumes containing no or almost no bubbles with those containing large bubble fractions close to the surface (depth $\leq$ 10 μm) provides qualitative information on the S-bearing species in the fluid. It is emphasized that the contribution of the S species in the bubbles to the spectra is very small and that the spectra are dominated by contributions of the surrounding S in the glass. However, as shown in Fig. D.1, few spectra reveal significant differences which may be attributed to S-species in the fluid phase. Fig. D.1 displays selected spectra of AHC-2 (~QFM+4, *r*: ~0.1 MPa/s, t_A: ~20 h; for details see Table 2 in Fiege et al.; 2014) and RED-3 (~QFM+1, ~0.1 MPA/s, ~5 h) collected on areas with very low volume fraction of bubbles (*g*) and on bubble-rich areas (*g*+*b*). Spectra of reference materials are plotted for comparison.

In general, differences in energy position and peak shape of bands related to S^{4+} and S^{2-} species in glasses (or fluids) when compared to the peak positions and shape observed in the reference materials (sodium sulfite Na_2SO_3 for S^{4+} and pyrrhotite $Fe_{1-X}S$ for S^{2-}) are related to the different stereochemical environment and, thus, depend on the chemical composition of the respective S compound (e.g., Fleet, 2005; Klimm et al., 2012).

The spectrum of AHC-2 collected on a bubble-poor area (*g*) indicates that nearly all S in the glass is present as sulfate ($S^{6+}/\Sigma S$ ~1) at oxidizing conditions (~QFM+4). On the other hand, spectra collected on areas with a high volume fraction of bubbles [(AHC-2 (*b*+*g*)] reveal an additional, small but distinct peak at ~2478.2 eV. This peak most likely refers to sulfite S^{4+} (see reference material; Backnaes et al., 2008; Wilke et al., 2008). Noteworthy, Backnaes et al. (2008) as well as Wilke et al. (2008) noted that S^{2-} and S^{6+} are the only significant S species observed in quenched silicate glasses. Furthermore, it is unlikely that the observed sulfite peak is caused by irradiation as the applied analytical approach allows us to distinguish between original and artificial features (see above; Appendix Section D). Hence, the peak at ~2478.2 eV can most probably be attributed to SO_2 in the

closed bubbles. Although the contribution of the S^{4+} peak is small in the spectra, it indicates that SO_2 may be the dominant S species in the fluid phase at QFM+4.

Under reducing conditions (~QFM+1; RED-3 spectra) the $S^{6+}/\Sigma S$ ratio was found to be remarkably lower in areas with high volume fraction of bubbles closed to the surface (*g*+*b*) when compared to bubble poor/free areas (*g*). The high abundance of the broad peak at ~2477 eV observed in the vesiculated area is probably related to S^{2-} species in the fluid phase. Hence, it is suggested that significant amounts of H_2S are present in the fluid phase at QFM+1.

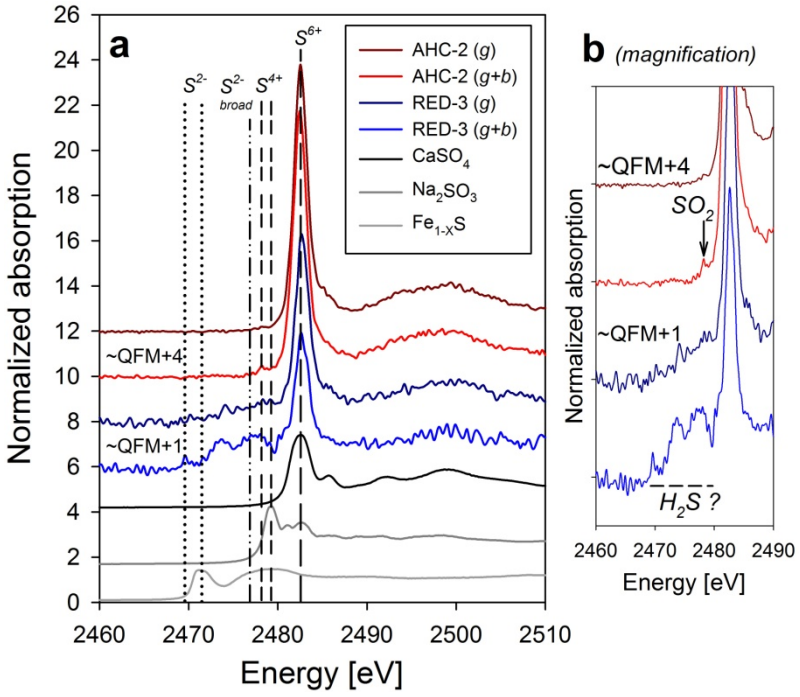

Fig. F.1 a/b: S Kα XANES spectra of selected experimental glasses and reference materials. **a)** The vertical lines mark the positions of the observed sulfur species. The spectra were collected with a beam size of about 60×60 µm, either on bubble free parts of the experimental samples (*g*; glass only) or on areas with a large volume fraction of bubbles close to the surface (*g*+*b*; glass and bubbles). The sharp peaks at 2482.2 eV, present in most displayed spectra, correspond to sulfate (S^{6+}, *long dashes*). The sharp but remarkably less prominent peak at 2478.2 eV (AHC-2 *g*+*b*) and 2479.2 eV (reference material: Na_2SO_3), respectively, indicates the presence of sulfite (S^{4+}, *short dashes*). The broad peak with a maximum at ~2477 eV can be attributed to sulfide (RED-3 *g*; RED-3 *g*+*b*; $Fe_{1-X}S$). The sharp peak observed at 2469.6 eV (RED-3 *g*+*b*) and at 2471.5 eV (reference material: $Fe_{1-X}S$) also refers to sulfide. The spectrum of sodium sulfite (Na_2SO_3, *dark grey*) indicates the presence of sulfate in the reference material, most likely related to irradiation caused by the X-ray beam (Wilke et al., 2008). **b)** Magnification of plot (**a**). The bands which may indicate the presence of SO_2 (at QFM+4) or H_2S (~QFM+1) in the fluid phase are marked by black arrow (SO_2) or dashed line (H_2S).
Note: Experiments AHC-2 was not analyzed by SIMS. Details about AHC-2 can be found in Table 2 of Fiege et al. (2014).

G. Modeling of equilibrium S isotope fractionation

The estimated fractionation pairs $\alpha(SO_{2\ gas} - SO_4^{2-}{}_{melt})$, $\alpha(SO_{2\ gas} - S^{2-}{}_{melt})$, $\alpha(H_2S_{\ gas} - S^{2-}{}_{melt})$ and $\alpha(H_2S_{\ gas} - SO_4^{2-}{}_{melt})$ are listed in Table 3 (see main text). These values were applied to calculate an average fractionation factors describing the S isotope fluid-melt fractionation for a given fO_2 at 1030°C [$\alpha_{g\text{-}m}(fO_2)$] using the following equation:

$$\alpha_{g\text{-}m}(fO_2) = A \cdot \alpha(SO_{2\ gas} - SO_4^{2-}{}_{melt}) + B \cdot \alpha(H_2S_{gas} - S^{2-}{}_{melt}) + C \cdot \alpha(SO_{2\ gas} - S^{2-}{}_{melt}) + D \cdot \alpha(H_2S_{\ gas} - SO_4^{2-}{}_{melt}) \quad \text{(eqn. A1)}$$

$A = x(SO_2)$ if $x(SO_2) \leq x(SO_4^{2-})$ otherwise $A = x(SO_4^{2-})$ (eqn. A1-1)

$B = x(H_2S)$ if $x(H_2S) \leq x(S^{2-})$ otherwise $B = x(S^{2-})$ (eqn. A1-2)

$C = 0$ if $x(SO_2) \leq x(SO_4^{2-})$ otherwise $C = x(SO_2) - x(SO_4^{2-})$ (eqn. A1-3)

$D = 0$ if $x(H_2S) \leq x(S^{2-})$ otherwise $D = x(H_2S) - x(S^{2-})$ (eqn. A1-4)

where $x(SO_4^{2-})$ is the molar fraction of sulfate in the melt, $x(S^{2-})$ the molar fraction of sulfide in the melt, $x(SO_2)$ the molar fraction of SO_2 in the fluid and $x(H_2S)$ the molar fraction of H_2S in the fluid.

Note: Our model approach yields identical trends as the approach of Sakai et al. (1982) if the same input parameters (i.e., S speciation, fractionation factors) are applied (see Section 5.2, main text).

H. Modeling the S speciation (melt and fluid)

The S speciation in the melt phase and the (coexisting) fluid phase can be estimated using different model approaches. In Fig. H.1 we compare S speciation trends calculated based on models used by, e.g., De Hoog et al. (2001) to more recent approaches (Burgisser et al., 2008; Jugo et al., 2010) applied in this study (see Section 5.2). The comparison indicates that *i)* the shape of the trend predicted by the approach of Wallace and Carmichael (1992) differs significantly from that of more recently proposed models and *ii)* the compositional dependence of the sulfide-sulfate transition is quite significant, which is in good agreement with, e.g., Baker and Moretti (2011). The *DCompress* model predicts a shift of the sulfide-sulfate transition by >0.5 log units towards more oxidizing conditions if a basaltic system

at 1030°C is compared to a rhyolitic system at 900°C. Considering this observation as well as the S speciation data provided by Fiege et al. (2014) for experimental run products also studied in this work, we suggest that the sulfide-sulfate transition within the andesitic melt of this study is probably at ~0.5 log units higher fO_2 than suggested by Jugo et al. (2010) for basaltic systems (see Fig. 7 and Section 5.2; main text).

1048

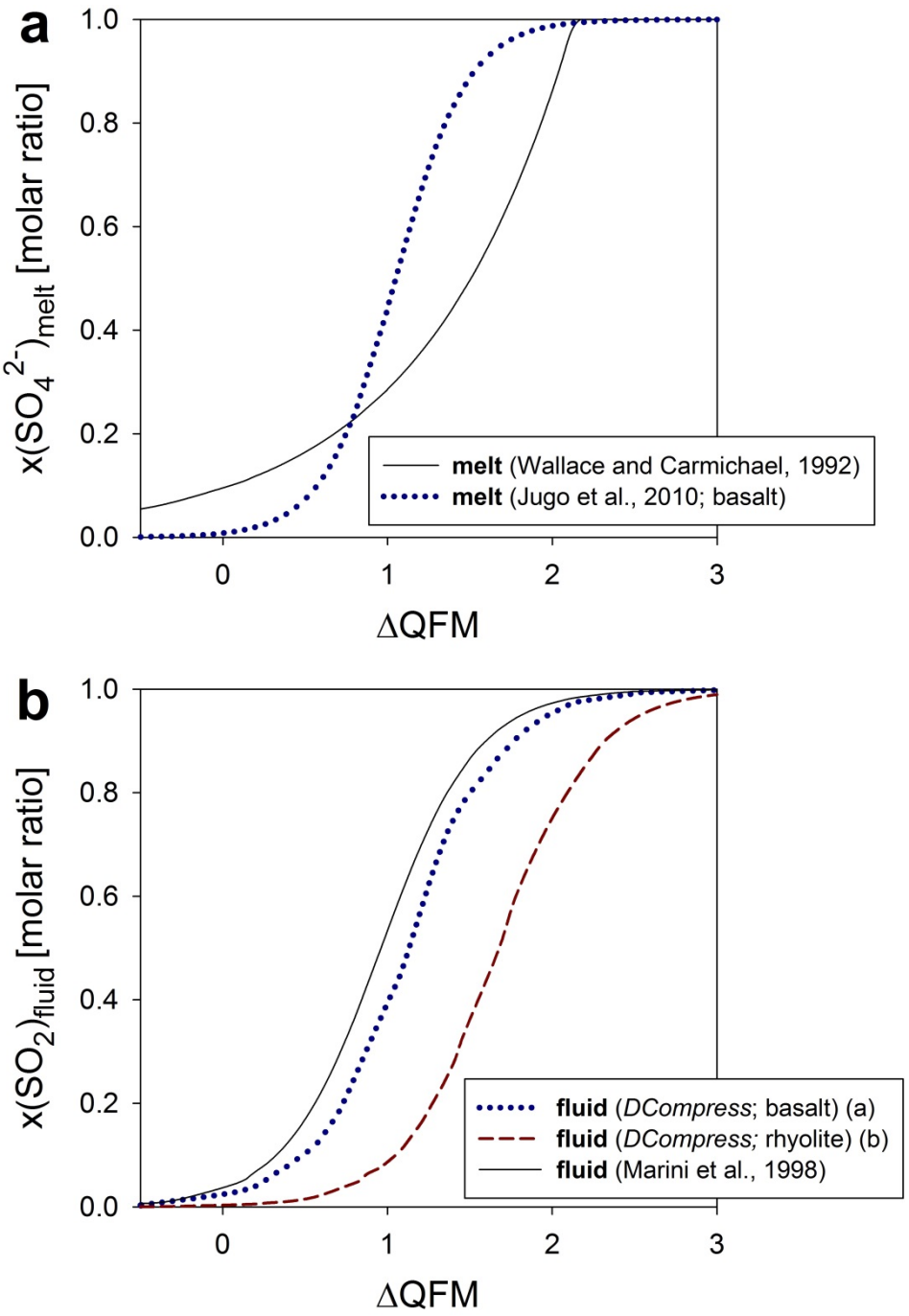

Fig. H.1 a/b: Modelling the S speciation in the aqueous fluids and silicate melts. **a)** Melt phase; trends calculated using the models of Jugo et al. (2010) and Wallace and Carmichael (1992), respectively; $x(SO_4^{2-})_{melt} = SO_4^{2-} / (SO_4^{2-} + S^{2-})$ [molar ratio]. **b)** Fluid phase; trends calculated using the *DCompress* progam (Burgisser et al., 2008; see text) and the model of Marini et al. (1998), respectively; $x(SO_2)_{fluid} = SO_2 / (SO_2 + H_2S)$ [molar ratio].
(a) The trend was predicted by *DCompress* for a basaltic melt containing initially 6 wt% H_2O, 1000 ppm S and 0.1 wt% gas at 300 MPa; final p = 70 MPa; T = 1030°C.
(b) The trend was predicted by *DCompress* for a rhyolitic melt containing initially 6 wt% H_2O, 1000 ppm S and 0.1 wt% gas at 300 MPa; final p = 70 MPa; T = 1030°C.

1049

REFERENCES USED IN THE APPENDIX

Backnaes L., Stelling J., Behrens H., Goettlicher J., Mangold S., Verheijen O., Beerkens R. G. C. and Deubener J. (2008) Dissolution mechanisms of tetravalent sulphur in silicate melts: Evidences from sulphur K edge XANES studies on glasses. *J. Am. Ceram. Soc.* **91**, 721-727.

Baker D. R. and Moretti R. (2011) Modeling the Solubility of Sulfur in Magmas: A 50-Year Old Geochemical Challenge. *Rev. Mineral. Geochem.* **73**, 167-213.

Botcharnikov R. E., Linnen R. L., Wilke M., Holtz F., Jugo P. J. and Berndt J. (2011) High gold concentrations in sulphide-bearing magma under oxidizing conditions. *Nat. Geosci.* **4**, 112-115.

Burgisser A., Scaillet B. and Harshvardhan (2008) Chemical patterns of erupting silicic magmas and their influence on the amount of degassing during ascent. *J. Geophys. Res.* **113**, B12204, 1-14.

Dimitrov V. and Komatsu, T. (2013) Electronic polarizability, optical basicity and single bond strength of oxide glasses. *J. Chem. Technol. Metall.* **48**, 549-554.

Fiege A., Behrens H., Holtz F. and Adams F. (2014) Kinetic vs. thermodynamic control of degassing of H_2O-S±Cl bearing andesitic melts. *Geochim. Cosmochim. Acta* **125**, 241-264.

Fleet M. E. (2005) XANES spectroscopy of sulfur in earth materials. *Can. Mineral.* **43**, 1811-1838.

Frost B. R. (1991) Introduction to Oxygen Fugacity and Its Petrological Importance. *Rev. Mineral.* **25**, 1-9.

Jugo P. J., Wilke M. and Botcharnikov R. E. (2010) Sulfur K-edge XANES analysis of natural and synthetic basaltic glasses: Implications for S speciation and S content as function of oxygen fugacity. *Geochim. Cosmochim. Acta* **74**, 5926-5938.

Klimm K., Kohn S. C., O'Dell L. A., Botcharnikov R. E. and Smith M. E. (2012) The dissolution mechanism of sulphur in hydrous silicate melts. I: Assessment of analytical techniques in determining the sulphur speciation in iron-free to iron-poor glasses. *Chem. Geol.* **322–323**, 237-249.

Mandeville C. W., Sasaki A., Saito G., Faure K., King R. and Hauri E. (1998) Open-system degassing of sulfur from Krakatau 1883 magma. **160**, 709-722.

Mandeville C. W., Webster J. D., Rutherford M. J., Taylor B. E., Timbal A. and Faure K. (2002) Determination of molar absorptivities for infrared absorption bands of H_2O in andesitic glasses. *Am. Mineral.* **87**, 813-821.

Marini L., Chiappini V., Cioni R., Cortecci G., Dinelli E., Principe C. and Ferrara G. (1998) Effect of degassing on sulfur contents and $\delta^{34}S$ values in Somma-Vesuvius magmas. *Bull. Volcanol.* **60**, 187-194.

Ohlhorst S., Behrens H. and Holtz F. (2001) Compositional dependence of molar absorptivities of near-infrared OH- and H_2O bands in rhyolitic to basaltic glasses. *Chem. Geol.* **174**, 5-20.

Rao K. J. (2002) *Structural Chemistry of Glasses*. Elsevier. 567 pp.

Sakai H., Casadevall T. and Moore J. G. (1982) Chemistry and isotope ratios of sulfur in basalts and volcanic gases at Kilauea volcano, Hawaii. *Geochim. Cosmochim. Acta* **46**, 729-738.

Sasaki A., Arikawa Y. and Folinsbee R. E. (1979) Kiba reagent method of sulfur extraction applied to isotopic work. *Bull. Geol. Surv. Jpn.* **30**, 241-245.

Silver L. A., Ihinger P. D. and Stolper E. (1990) The influence of bulk composition on the speciation of water in silicate glasses. *Contrib. Mineral. Petrol.* **104**, 142-162.

Stelling J., Behrens H., Wilke M., Göttlicher J. and Chalmin-Aljanabi E. (2011) Interaction between sulphide and H_2O in silicate melts. *Geochim. Cosmochim. Acta* **75**, 3542-3557.

Tichý L. and Tichá H. (1995) Covalent bond approach to the glass-transition temperature of chalcogenide glasses. *J. Non-Cryst. Solids.* **189**, 141-146.

Wallace P. and Carmichael I. S. E. (1992) Sulfur in Basaltic Magmas. *Geochim. Cosmochim. Acta* **56**, 1863-1874.

Wilke M., Jugo P. J., Klimm K., Susini J., Botcharnikov R., Kohn S. C. and Janousch M. (2008) The origin of S^{4+} detected in silicate glasses by XANES. *Am. Mineral.* **93**, 235-240.

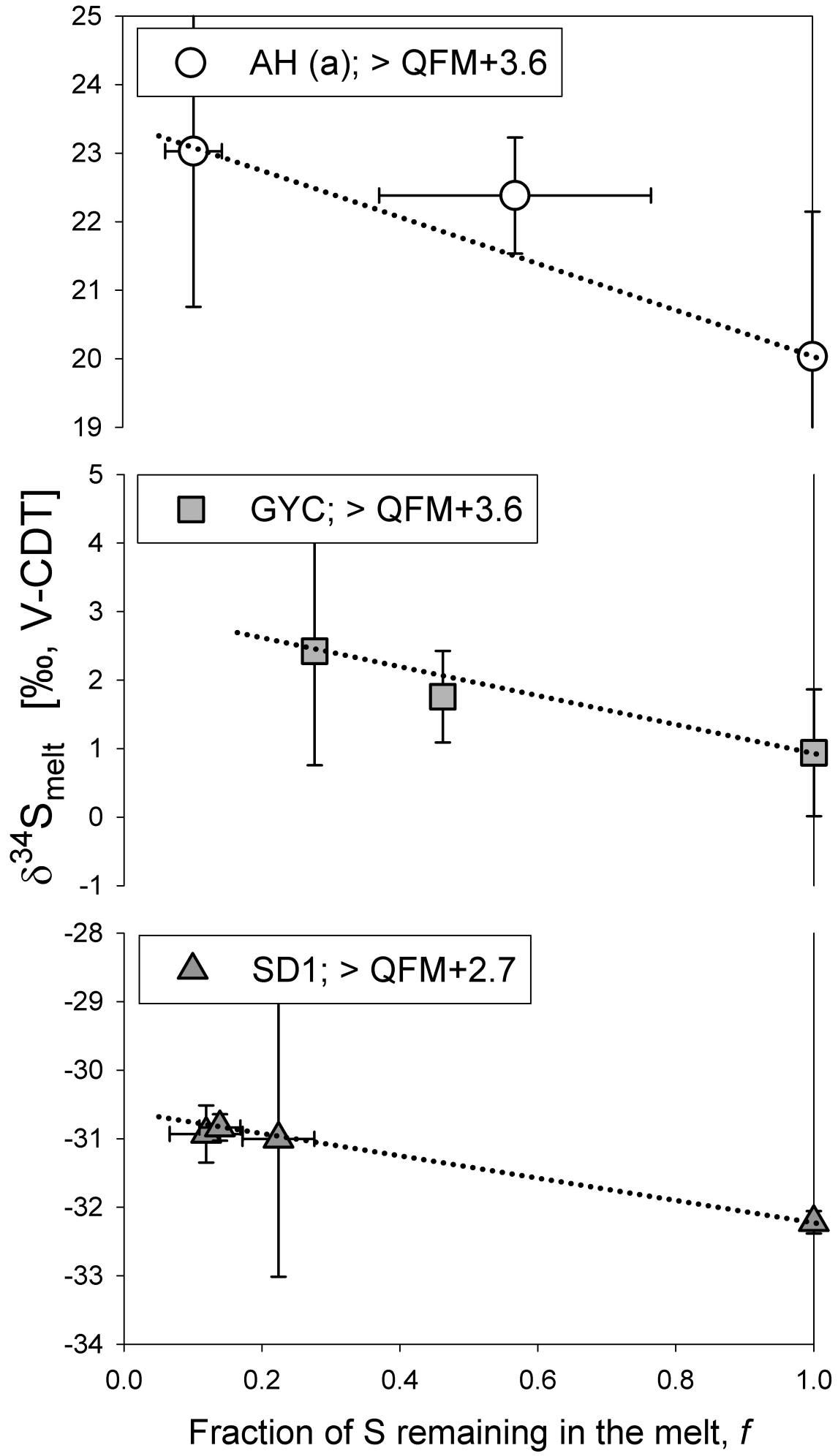
AH (a); > QFM+3.6
GYC; > QFM+3.6
SD1; > QFM+2.7
δ34Smelt [‰, V-CDT]
Fraction of S remaining in the melt, f
25
24
23
22
21
20
19
5
4
3
2
1
0
-1
-28
-29
-30
-31
-32
-33
-34
0.0
0.2
0.4
0.6
0.8
1.0

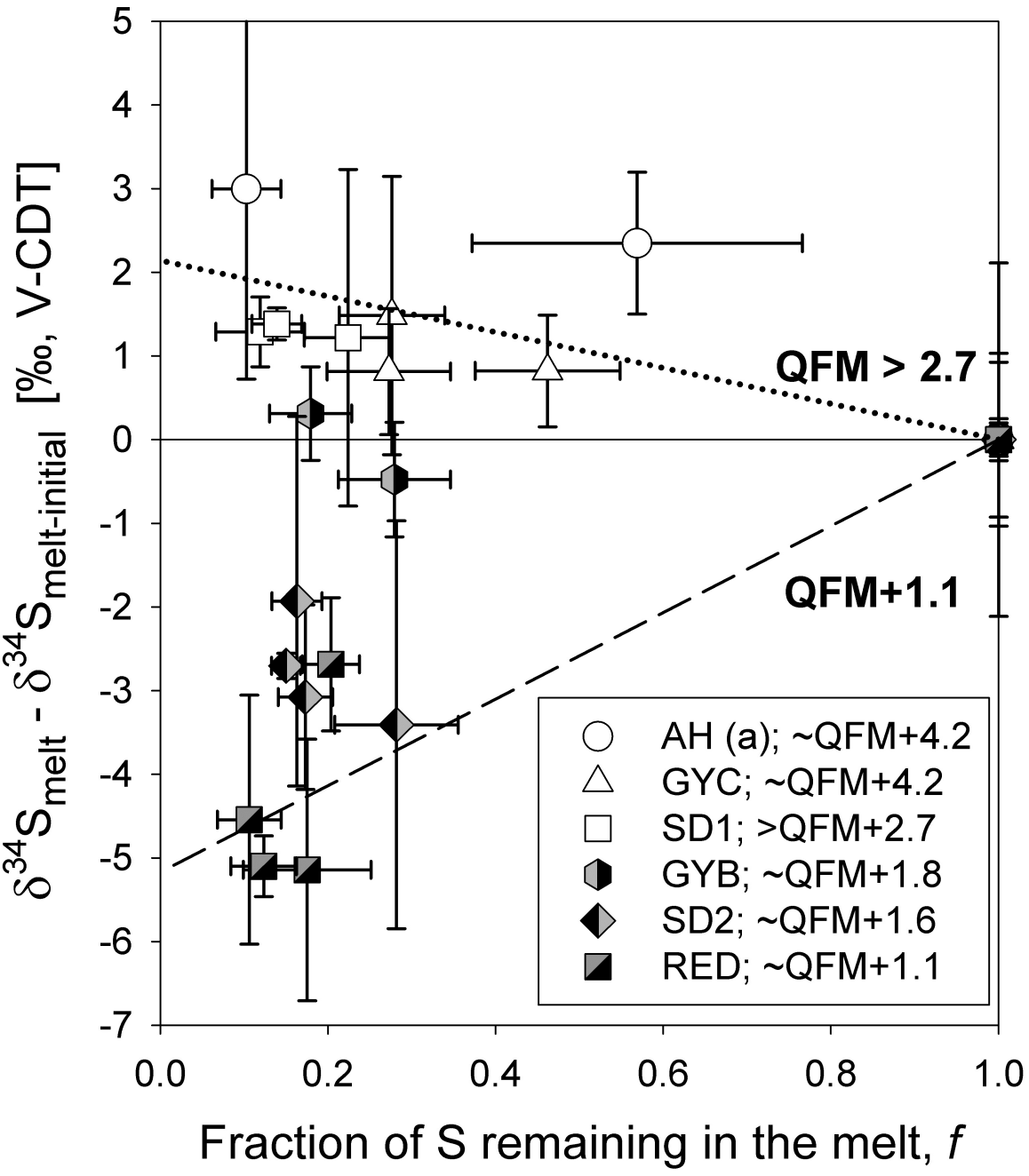
5
4
3
2
1
0
-1
-2
-3
-4
-5
-6
-7
0.0
0.2
0.4
0.6
0.8
1.0
$\delta^{34}S_{melt} - \delta^{34}S_{melt\text{-}initial}$ [‰, V-CDT]
Fraction of S remaining in the melt, *f*
QFM > 2.7
QFM+1.1
AH (a); ~QFM+4.2
GYC; ~QFM+4.2
SD1; >QFM+2.7
GYB; ~QFM+1.8
SD2; ~QFM+1.6
RED; ~QFM+1.1

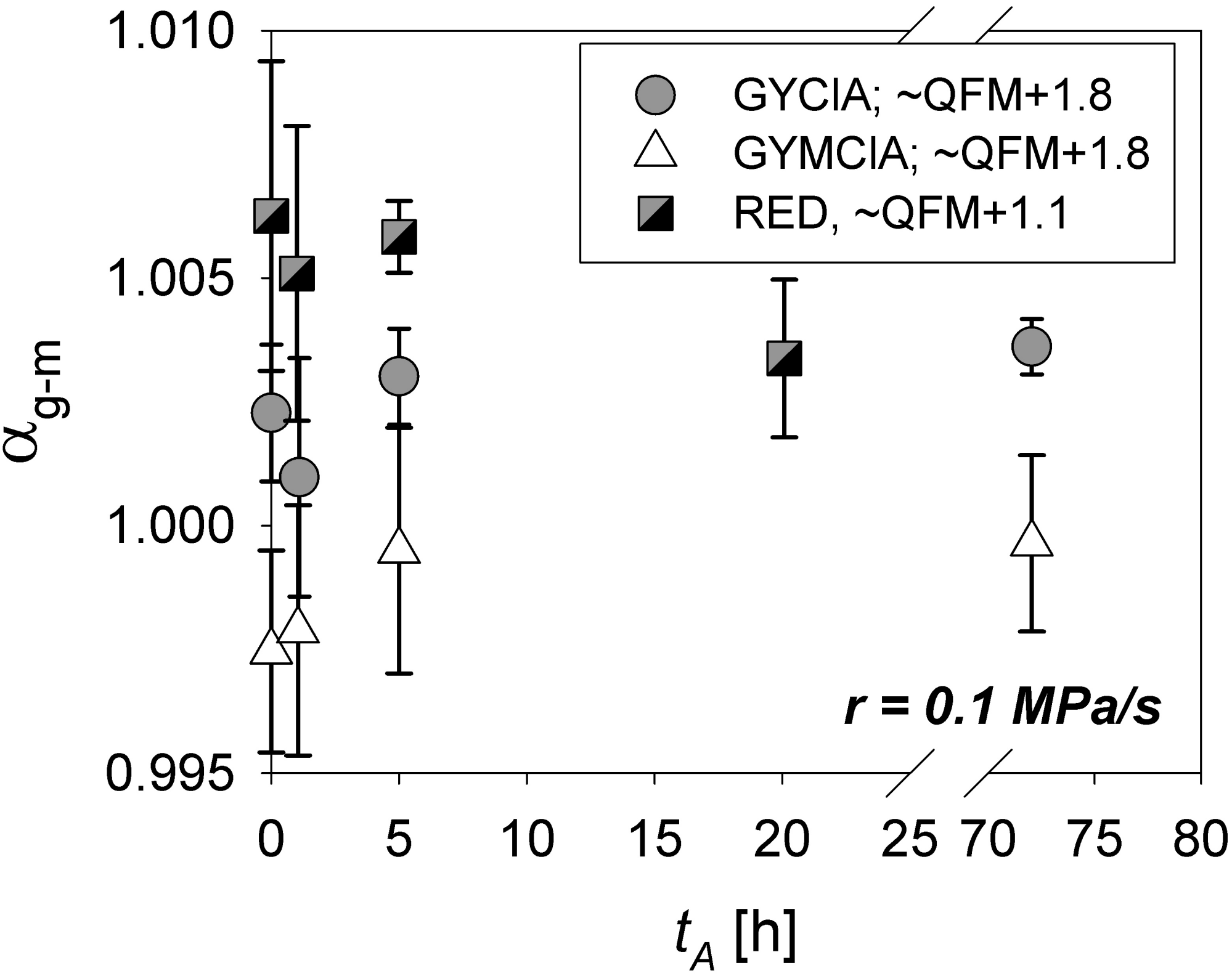
1.010
1.005
1.000
0.995
$\alpha_{g\text{-}m}$
GYCIA; ~QFM+1.8
GYMCIA; ~QFM+1.8
RED, ~QFM+1.1
r = 0.1 MPa/s
0
5
10
15
20
25
70
75
80
t_A [h]

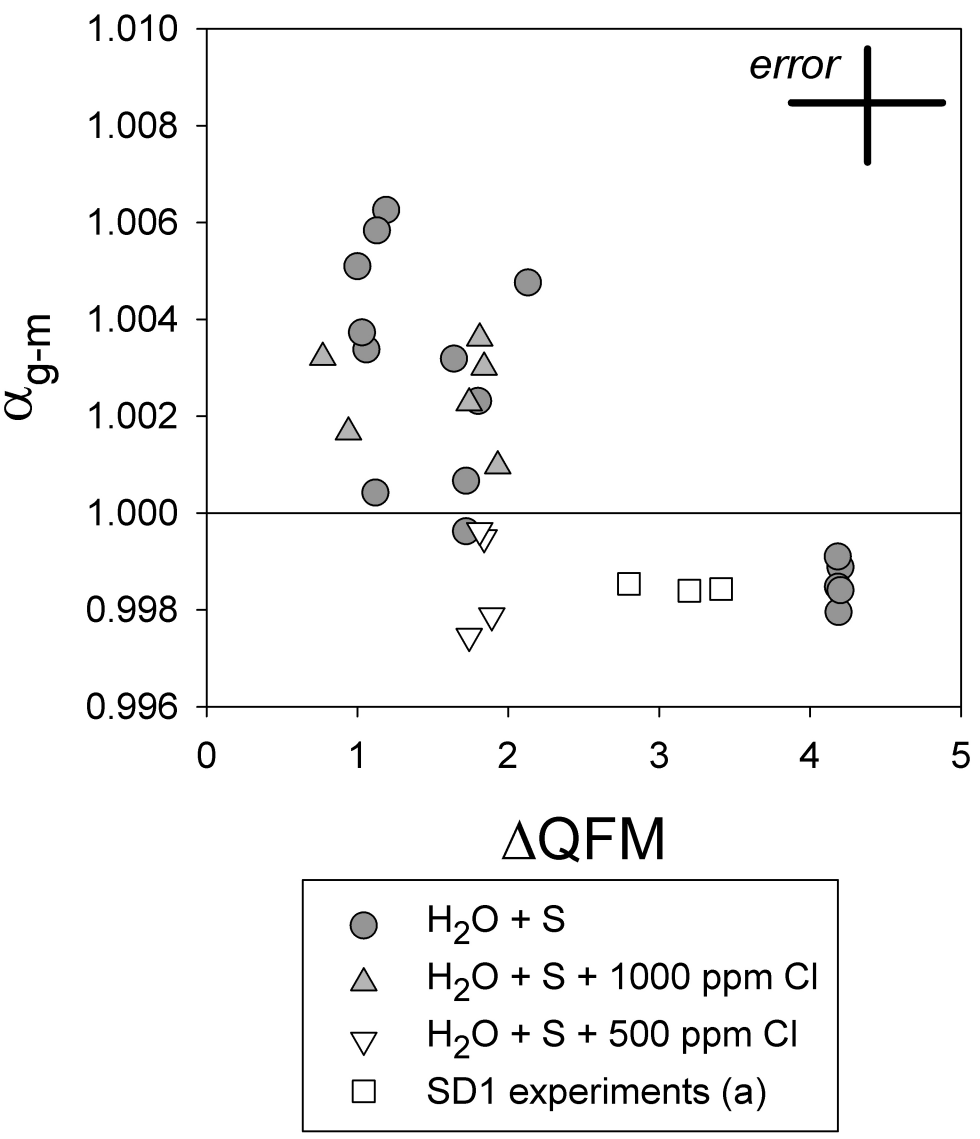
error
1.010
1.008
1.006
1.004
1.002
1.000
0.998
0.996
$\alpha_{g\text{-}m}$
0
1
2
3
4
5
ΔQFM
H_2O + S
H_2O + S + 1000 ppm Cl
H_2O + S + 500 ppm Cl
SD1 experiments (a)

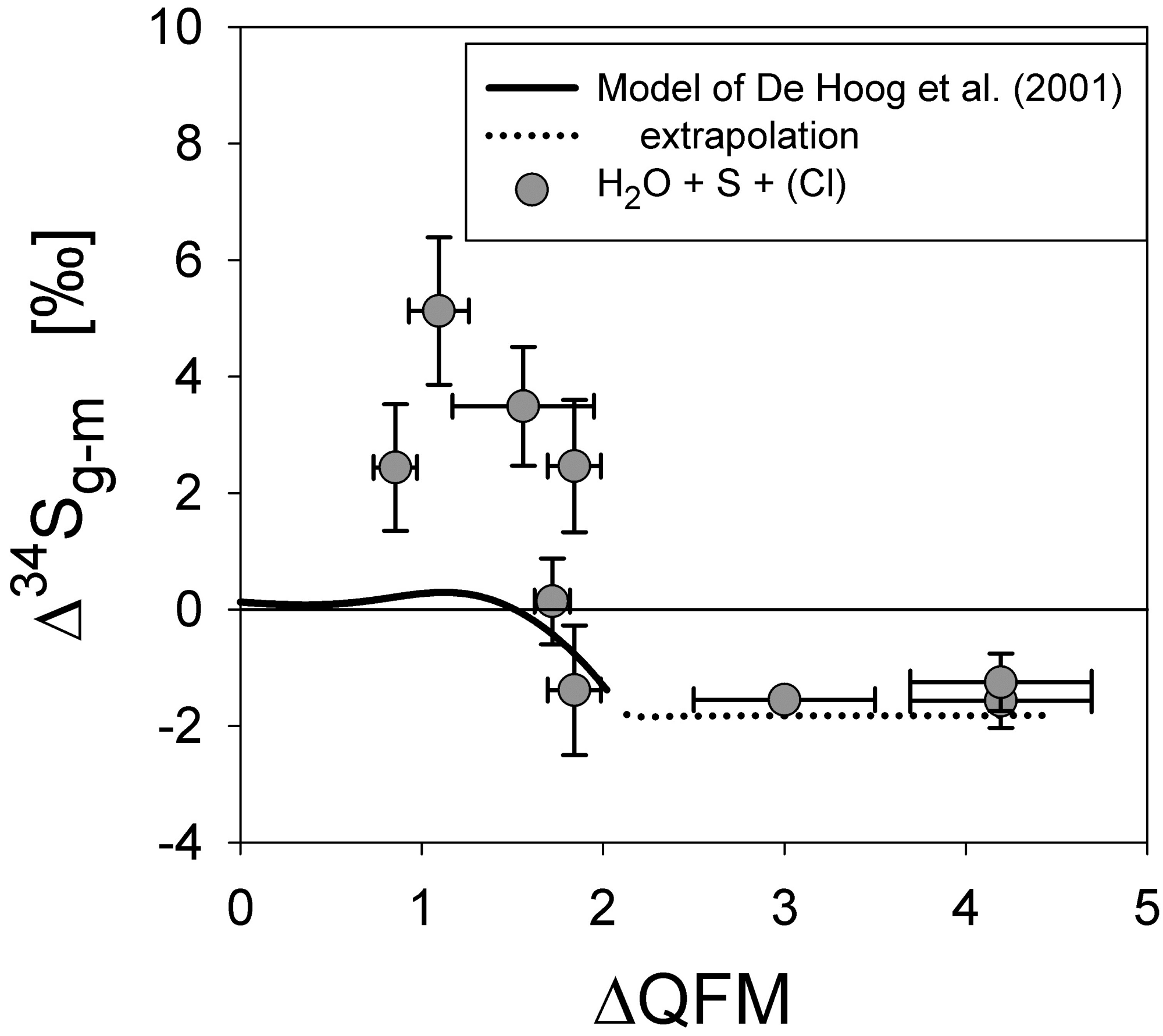
Model of De Hoog et al. (2001)
extrapolation
H2O + S + (Cl)
10
8
6
4
2
0
-2
-4
0
1
2
3
4
5
Δ34Sg-m [‰]
ΔQFM

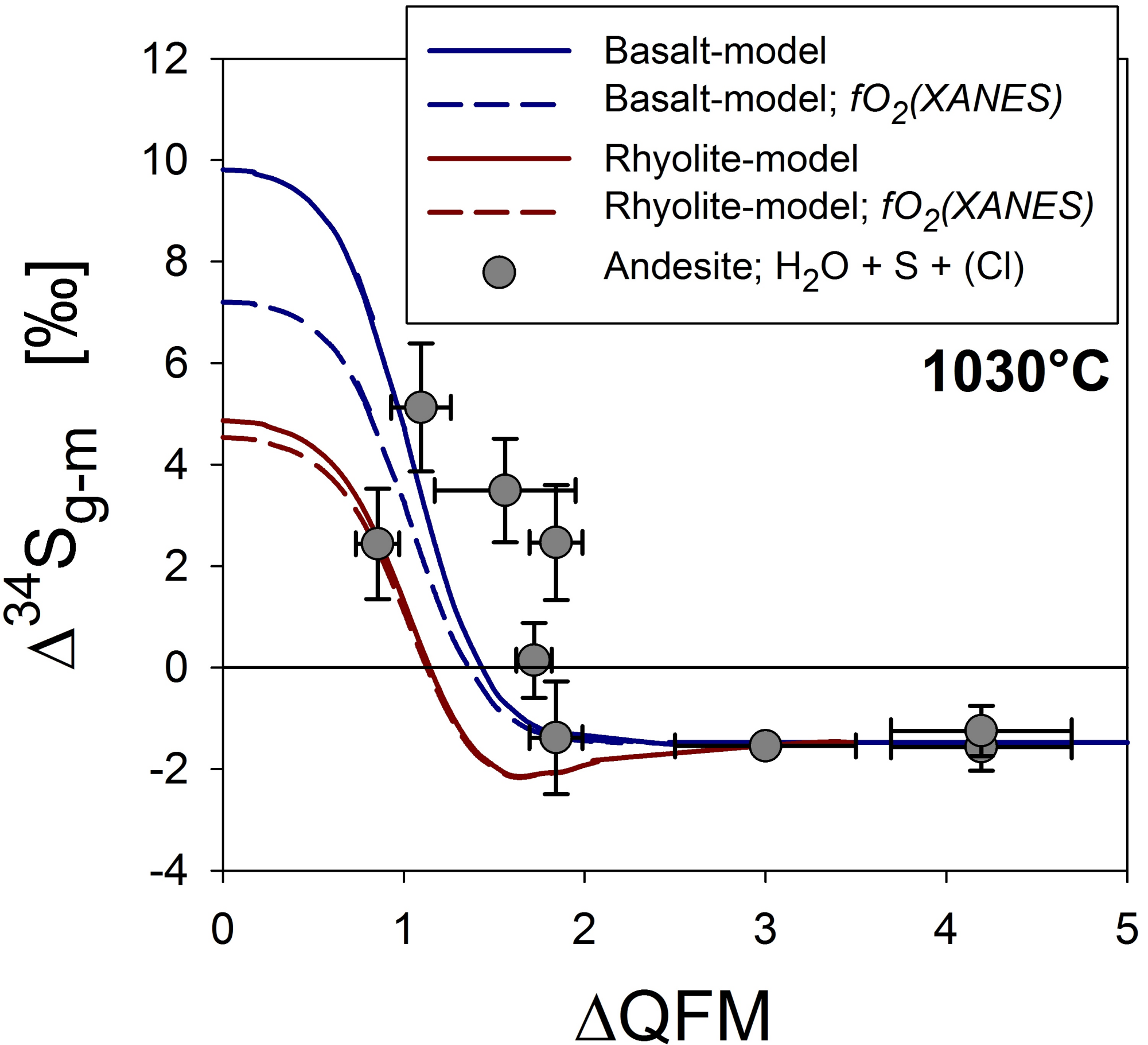
Basalt-model
Basalt-model; fO_2(XANES)
Rhyolite-model
Rhyolite-model; fO_2(XANES)
Andesite; H_2O + S + (Cl)
1030°C
$\Delta^{34}S_{g-m}$ [‰]
ΔQFM
12
10
8
6
4
2
0
-2
-4
0
1
2
3
4
5

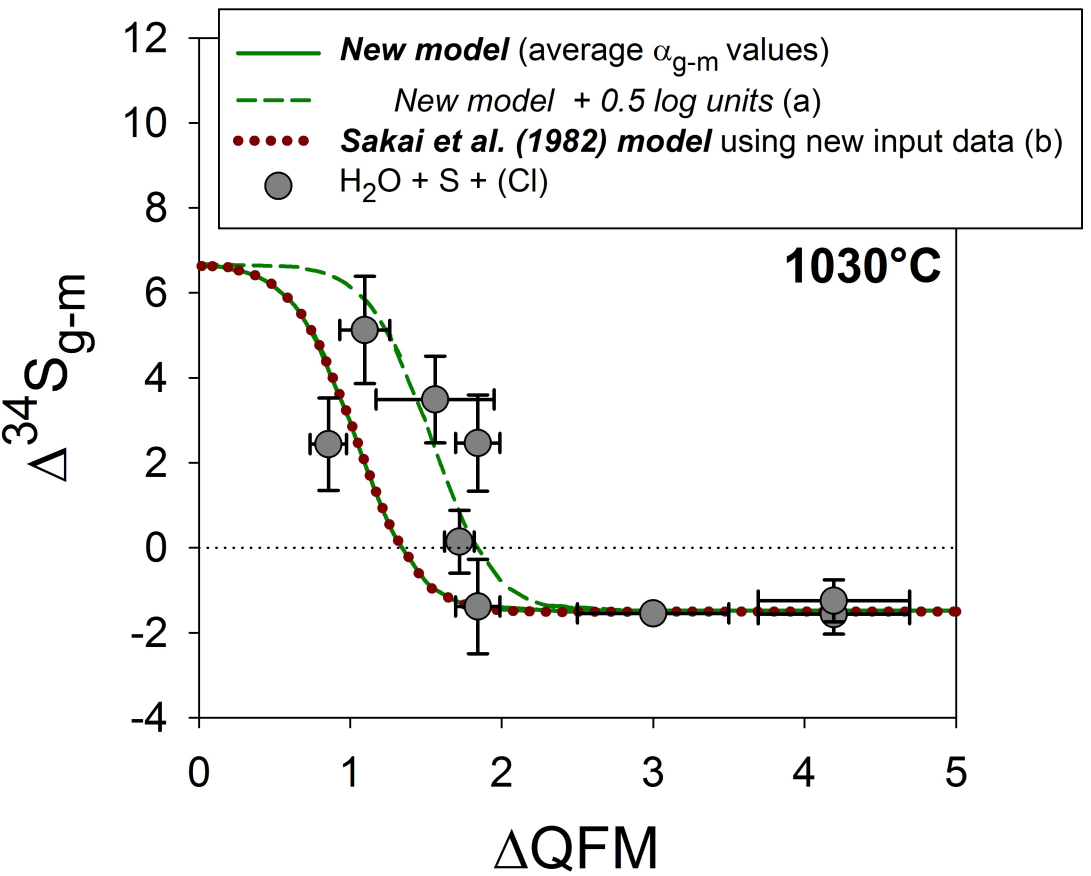
New model (average $\alpha_{g\text{-}m}$ values)
New model + 0.5 log units (a)
Sakai et al. (1982) model using new input data (b)
H_2O + S + (Cl)
1030°C
$\Delta^{34}S_{g\text{-}m}$
ΔQFM
12
10
8
6
4
2
0
-2
-4
0
1
2
3
4
5

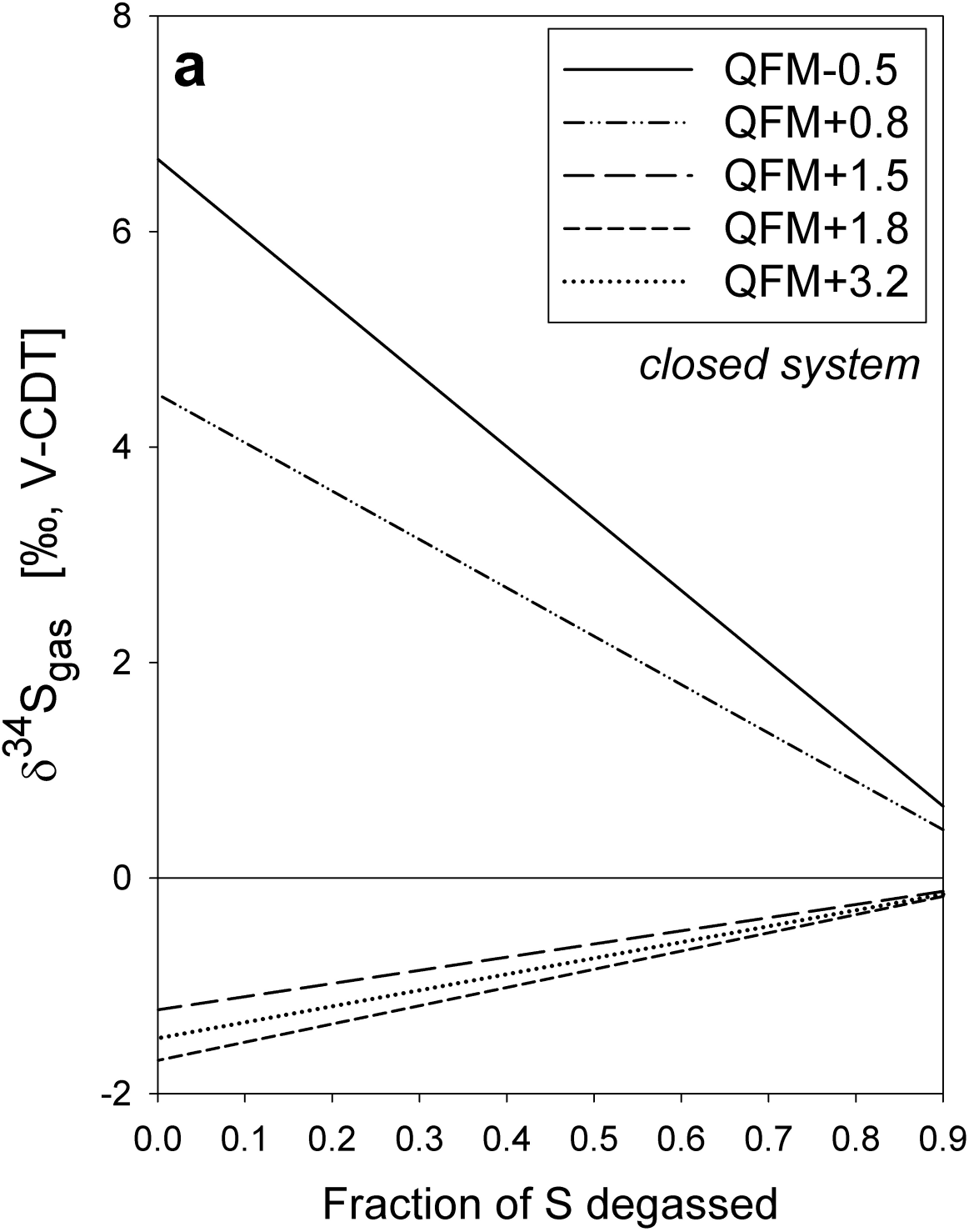
a
QFM-0.5
QFM+0.8
QFM+1.5
QFM+1.8
QFM+3.2
closed system
8
6
4
2
0
-2
$\delta^{34}S_{gas}$ [‰, V-CDT]
0.0
0.1
0.2
0.3
0.4
0.5
0.6
0.7
0.8
0.9
Fraction of S degassed

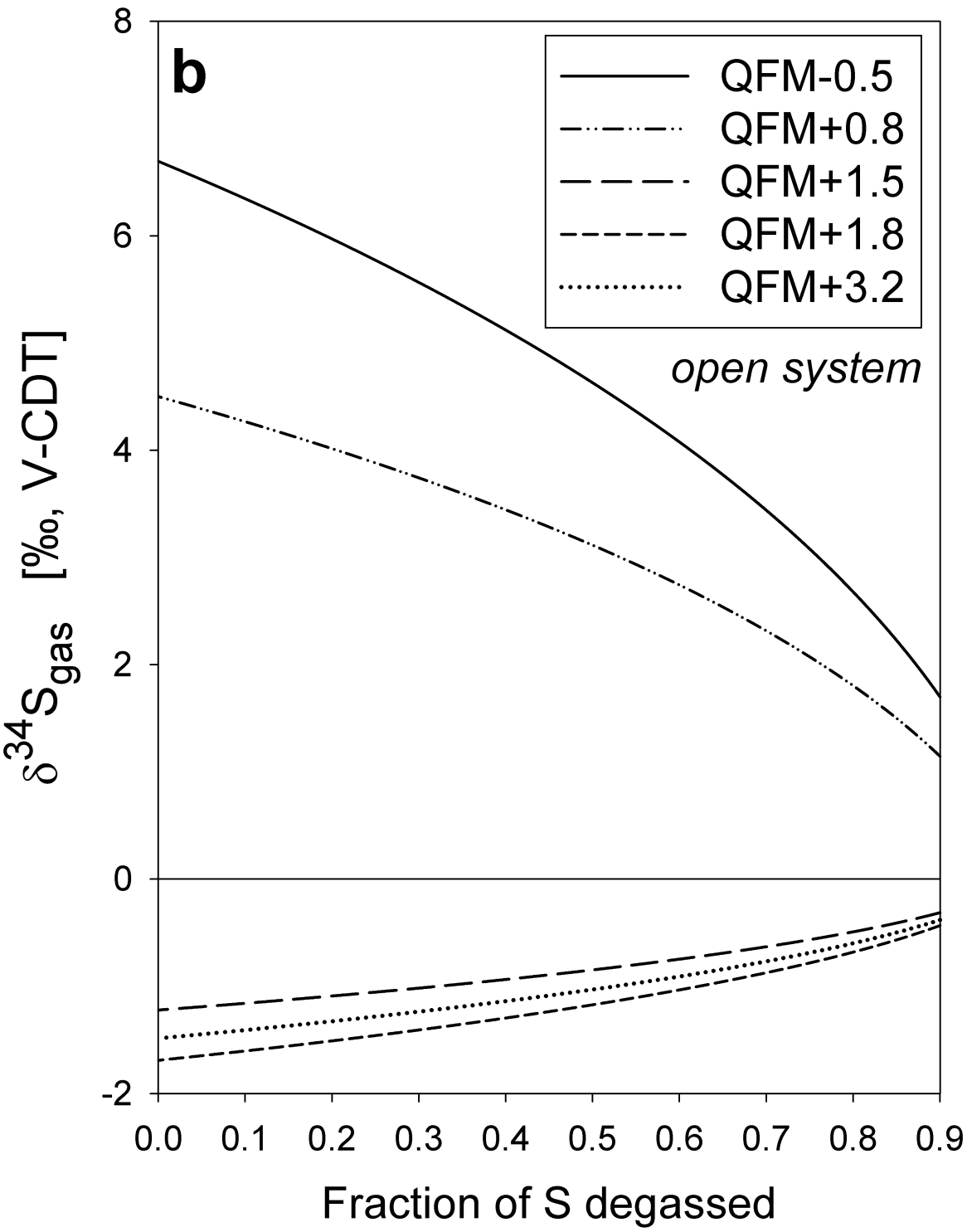
b
QFM-0.5
QFM+0.8
QFM+1.5
QFM+1.8
QFM+3.2
open system
8
6
4
2
0
-2
$\delta^{34}S_{gas}$ [‰, V-CDT]
0.0
0.1
0.2
0.3
0.4
0.5
0.6
0.7
0.8
0.9
Fraction of S degassed